$^{40}Ar/^{39}Ar$ age constraints on the formation of fluid-rich quartz veins from the NW Rhenohercynian zone (Rursee area, Germany)

Akbar Aydin Oglu Huseynov[1*], Jan R. Wijbrans[1], Klaudia F. Kuiper[1] & Jeroen van der Lubbe [1]

[1]Vrije Universiteit Amsterdam, De Boelelaan 1085, 1081HV Amsterdam, the Netherlands

Correspondence to: Akbar Aydin Oglu Huseynov (a.huseynov@vu.nl)

Abstract. The late Palaeozoic Variscan orogeny (~350 Ma) dictates a significant part of the subsurface geology in north-western and central Europe. Our focus is particularly on veining that occurred in metamorphosed sedimentary rocks that are affected by this orogeny. Vein minerals serve as repositories for documenting the origin of subsurface fluid flows and dynamics, and dating them provides crucial insight into the timing of orogenic and possible reactivation events. The Rursee area (Rhenish Massif, Germany) that is part of the Variscan foreland zone on the Avalonia micro-continent represents a key locality for studying Variscan quartz vein formation. Based on structural grounds, the two different groups/types of Rursee quartz veins have been linked with the early stages of Variscan, but their absolute ages are still unknown.

The aim of this study is to date these quartz veins using the $^{40}Ar/^{39}Ar$ stepwise crushing method based on the radioactive decay of ^{40}K dissolved in high salinity fluid inclusions. We obtained Jurassic to Cretaceous ages, and the isotopic analysis of argon gases revealed that the fluid-rich quartz fractions release ^{39}Ar in two distinct phases. Regardless of quartz veins fluid inclusions salinity, stepwise crushing provides apparent K/Cl >1. Electron Probe Micro Analyser data confirm the presence of the K (^{39}Ar) in the K-bearing mineral inclusions (e.g., sericite, mica, and chlorite) and in microcracks and possibly in the crystal lattice of quartz.

K-bearing mineral inclusions and/or crystal lattice of quartz, which form in the Variscan-origin vein fractures, provide a plausible explanation for the young apparent isotopic ages. The presence of the quartz sub-grains may suggest that obtained maximum apparent ages are likely to reflect post-Variscan reactivation-recrystallisation due to tectonic activity or its cooling moment during the Jurassic-Cretaceous period rather than the original Variscan vein formation.

This study emphasizes the complexities of isotopic dating of fluid inclusions, as well as the importance of careful interpretation of such data, especially in cases where different K-bearing mineral inclusions and/or radiogenic argon from crystal lattice obscure the initial fluid inclusions signal.

1 Introduction

Quartz veins are abundant in metamorphosed terranes and sedimentary basins filled with siliciclastic sediments, witnessing significant fluid movement during diagenesis and metamorphism (Yardley, 1983; Mullis et al., 1994; Cartwright & Buick, 2000; Oliver & Bons, 2001). Increase in both temperature and pressure during burial diagenesis, orogenesis and deformation

cause sedimentary and volcanic rocks to lose their volatile components and to release warm fluids, which cumulate minerals in fractures and faults (Baumgartner & Ferry, 1991; Yardley & Bottrell, 1993; Oliver & Bons, 2001; Cox, 2007). These often saline fluids contain, among others, $KCl_{(aq)}$ or $K_2CO_{3\,(aq)}$ (Rauchenstein-Martinek et al., 2014), which are partly precipitated during crystallisation of minerals in veins or as inclusions in these minerals (Sterner et al., 1988). One of the isotopes of potassium, ^{40}K, is radioactive and can be used for K-Ar or its derivative $^{40}Ar/^{39}Ar$ dating. Progressive crushing techniques enable to liberate gasses from fluid inclusions, mineral inclusions and/or crystal lattice for the age determination of geological events provided that K-concentrations are high enough (Qiu & Dai, 1989; Turner & Bannon, 1992; Turner & Wang, 1992; Qiu, 1996; Kendrick et al., 2001; Qiu & Wijbrans, 2006; Kendrick et al., 2006; Qiu & Wijbrans, 2008; Qiu & Jiang, 2007; Jiang et al., 2012; Bai et al., 2013; Liu et al., 2015). This method does not only define an age, but also quantifies the ratio of noble gases (e.g. $^{39}Ar_K/^{37}Ar_{Ca}$, $^{39}Ar_K/^{38}Ar_{Cl}$) derived from Ca, K and Cl, respectively, that have been formed during neutron radiation prior to analysis. The $^{39}Ar_K/^{38}Ar_{Cl}$ provides important information on the composition of parental fluids and their sources (Sumino et al., 2011; Cartwright et al., 2013). Beyond studies on fluid composition and provenance (Kelley et al.,1986; Turner & Bannon, 1992: Kendrick et al., 2001, 2006), the initial $^{40}Ar/^{36}Ar$ values of fluid inclusions in quartz can considerably vary and may be used to differentiate between meteoric-sourced water (~298.6) (Ballentine et al., 2002; Ozima & Podosek, 2002) and deeper crustal or mantle-derived fluids (>10,000; MORB >40,000) (Burnard et al., 1997). Additionally, hydrothermal waters can present sub-atmospheric $^{40}Ar/^{39}Ar$ ratios, as can be deduced from inverse isochrons of fluid-altered rocks (e.g. 280-290; Baksi, 2007).

In order to accurately determine the age of fluid inclusions in quartz veins using the $^{40}Ar/^{39}Ar$ stepwise crushing method or the source of the fluid based on $^{40}Ar/^{36}Ar$ ratios, it is necessary to consider three distinct components of ^{40}Ar, namely (1) radiogenic $^{40}Ar_R$ or $^{40}Ar^*$, which is produced in the sample itself through the radioactive decay of ^{40}K, and (2) ^{40}Ar that was initially trapped in the fluid inclusion, either as (2a) atmospheric $^{40}Ar_A$ or (2b) excess $^{40}Ar_E$. It has been posited that the presence of $^{40}Ar_E$ in fluid inclusions could create a challenge to determining accurate vein formation ages using the K-Ar dating technique (Rama et al., 1965). More recently, isochron diagrams using $^{40}Ar/^{39}Ar$ geochronology help to overcome this issue (McKee et al., 1993; Qiu, 1996; Qiu et al., 2002). In addition to $^{40}Ar_E$, the origin of $^{39}Ar_K$ (or K content) has been a topic of debate, with the possibility that the $^{39}Ar_K$ (and thus K) may come from the dissolved salts in fluid inclusions, leaking from the crystals lattice during crushing (Kendrick et al., 2011), and/or from any K-bearing mineral inclusions trapped inside the crystals (Qiu & Wijbrans, 2006; Kendrick, 2007; Qiu & Wijbrans, 2009; Kendrick & Phillips, 2009).

This study aims i) to determine the absolute age of quartz vein formation by analysing fluid inclusions using the stepwise crushing $^{40}Ar/^{39}Ar$ dating method, ii) to elucidate the location of K in the vein minerals (e.g., fluid inclusions, mineral inclusions, and/or crystal lattice) and iii) to identify when different K sources release their $^{39}Ar_K$ through the examination of released argon gases during the crushing process and geochemical analysis of quartz mineral samples using an Electron Probe Micro Analyser (EPMA).

Quartz samples were obtained from an outcrop near the Rursee in the upper reaches of the Rur river in the North Eifel region of Western Germany. Detailed structural investigations of this area have been previously conducted by Van Noten et al. (2007),

who differentiated quartz veins into two groups. The older generation of quartz veins, the so-called bedding normal veins (BNVs) is assigned to the early stages of the Variscan orogeny, whereas the second group, comprising bedding parallel veins (BPVs), is linked to the main stage of the Variscan orogeny. Absolute $^{40}Ar/^{39}Ar$ ages of fluid inclusions representing the age of quartz vein formation would allow us to better constrain the structural evolution and subsurface fluid flow during the Variscan orogeny in north-western Europe. Reliable $^{40}Ar/^{39}Ar$ age constraints of quartz vein formation would provide the opportunity to understand the timing and evolution of mountain building in analogue fold-and-thrust belts.

1.1 Geological Setting

The Rhenohercynian fold-and-thrust belt, part of the Variscan, is primarily located in the Rhenish Massif in Germany and extends westward into the Ardennes, southwest England, and eastward to the Harz Mountains (Kołtonik et al., 2018). The Ardennes Allochthone (Fig. 1a), western part of Rhenish Massif, structurally comprises three main components: the Dinant fold-and-thrust belt, the Lower Palaeozoic Inliers, and the High-Ardennes Slate Belt (HASB). The HASB primarily consists of Lower Devonian metasediments including the Rurberg (upper Pragian) and Heimbach (upper Pragian to lower Emsian) units.

For this study, quartz veins samples were collected near the Schwammenauel dam in the Rursee area of the North Eifel region, Germany (Fig. 1b). The Rurberg and Heimbach units feature alternating layers of siltstones and fine- to coarse-grained sandstones (Goemaere & Dejonghe, 2005), deposited in shallow marine to deltaic environments in the northern Rhenohercynian Ocean (Oncken et al., 1999). The Early Devonian strata have accumulated to a total thickness of up to 7 km due to rapid subsidence and deposition (Winterfeld, 1994) forming the Eifel syncline (Fig. 1b). These strata are overlain by a ~3 km thick sequence of Lower Lochkovian to Pragian deposits.

The late Carboniferous deformation of the Variscan foreland led to initial burial metamorphism (Mansy et al., 1999), with prehnite-pumpelleyite facies similar to the anchizone conditions in the North Eifel area (Fielitz 1995), where temperatures reached up to 220 °C (Littke et al., 2012). There is also evidence of the upward migration of warm fluids into the northern Variscan front in Ardennes, driven by Variscan thrusting (Muchez et al., 2000; Schroyen & Muchez, 2000; Lünenschloss et al., 2008).

Following the Variscan period, the Rhenish Massif has been affected by transpressional and transtensional deformation that resulted in the formation of complex fault networks that host vein mineralization (Franzke & Anderle, 1995; Ziegler & Dèzes, 2005). During the Jurassic-Cretaceous period, the southern Rhenish Massif was periodically affected by hydrothermal activities (Kirnbauer et al., 2012), as indicated by geochronological data for post-Variscan vein mineralization (Bonhomme et al., 1983; Mertz et al., 1986; Bähr, 1987; Jakobus, 1992; Hein & Behr, 1994; Klügel, 1997; Schneider & Haack, 1997; Glasmacher et al., 1998; Schneider et al., 1999; Chatziliadou & Kramm, 2009).

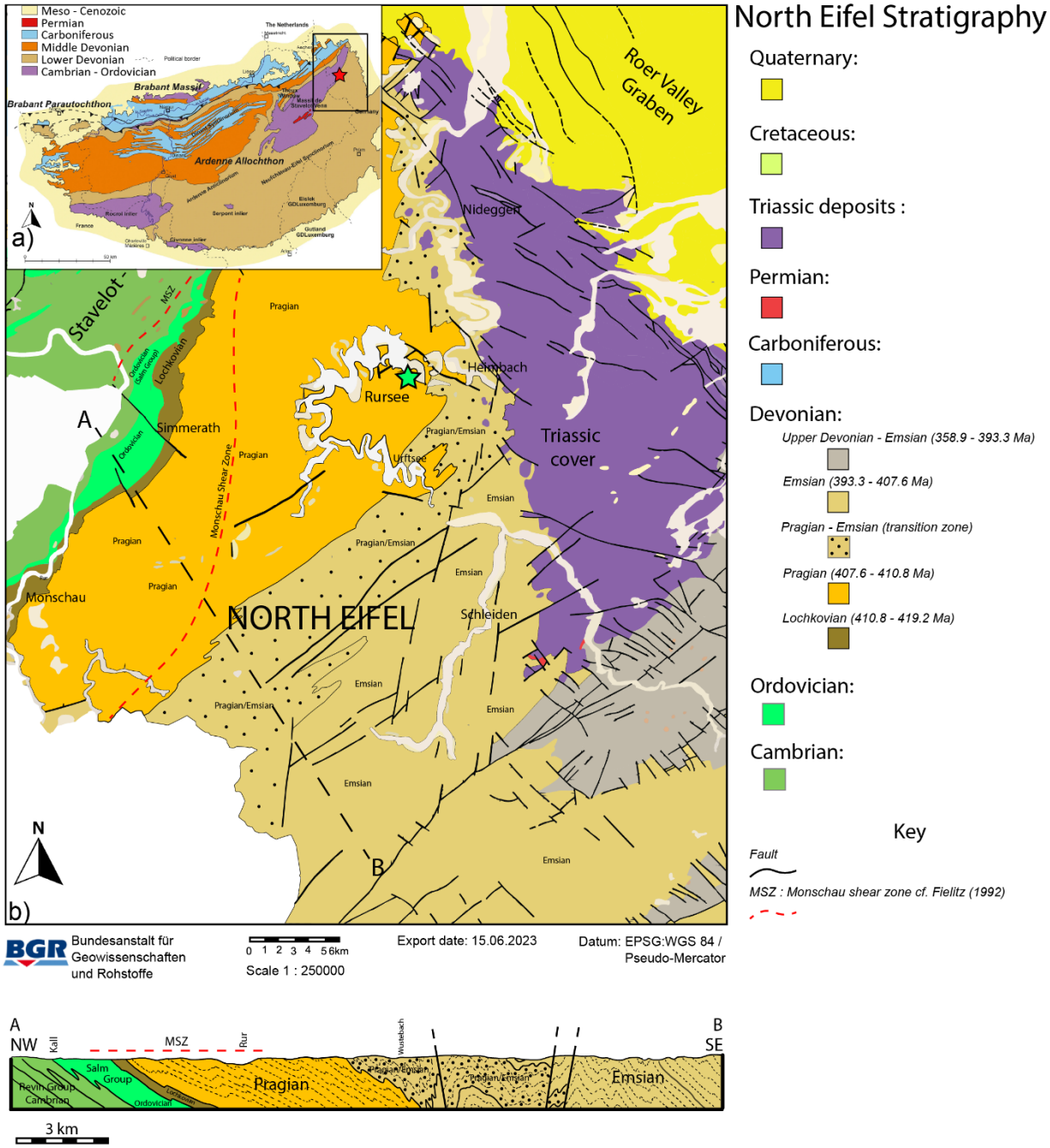

Figure 1: (a) Geological map with the Variscan frontal zone in the Ardenne-Eiffel region (study area marked with a red star). (b) Geological map of the North Eifel region (modified after Ribbert, 1992; Van Noten et al., 2011). The Lower Devonian layers overlay metamorphic deposits of the Lower Palaeozoic Stavelot-Venn Inlier. These layers have been locally distorted in the Monschau Shear Zone (MSZ), as documented by Fielitz (1992). Triassic sediments overlay the Lower Devonian layers in the eastern region. The sample location, indicated by a green star, is situated next to the Rursee reservoir, which is near the Schwammenauel dam. Below, cross-section illustrates the continuous northwest-southeast trending overturned folds that are characteristic of the North Eifel zone.

The $^{40}Ar/^{39}Ar$ study targets the BNVs and BPVs (Fig. 2), which formed in low-grade metamorphosed (prehnite-pumpelleyite facies) conditions as a result of the precipitates from warm fluids in fractures (Van Noten et al., 2008). The structural cross-cutting relationships between these quartz vein generations suggest that they originated during different geological events (Van Noten et al., 2008) revealing that BPVs are younger than BNVs. BNVs are found mostly within the competent psammite and hardly occur in incompetent pelitic layers. This positioning suggests that BNVs formed during the early stages of the Variscan orogeny, associated with the final burial phases of the Ardennes-Eifel basin (Sintubin et al., 2000; Urai et al., 2001; Van Noten et al., 2008, 2009).

In contrast, BPVs follow the strata between the psammatic and pelitic layers as a result of the bedding-parallel slip caused by flexural folding during the Variscan orogeny (Van Noten et al., 2008).

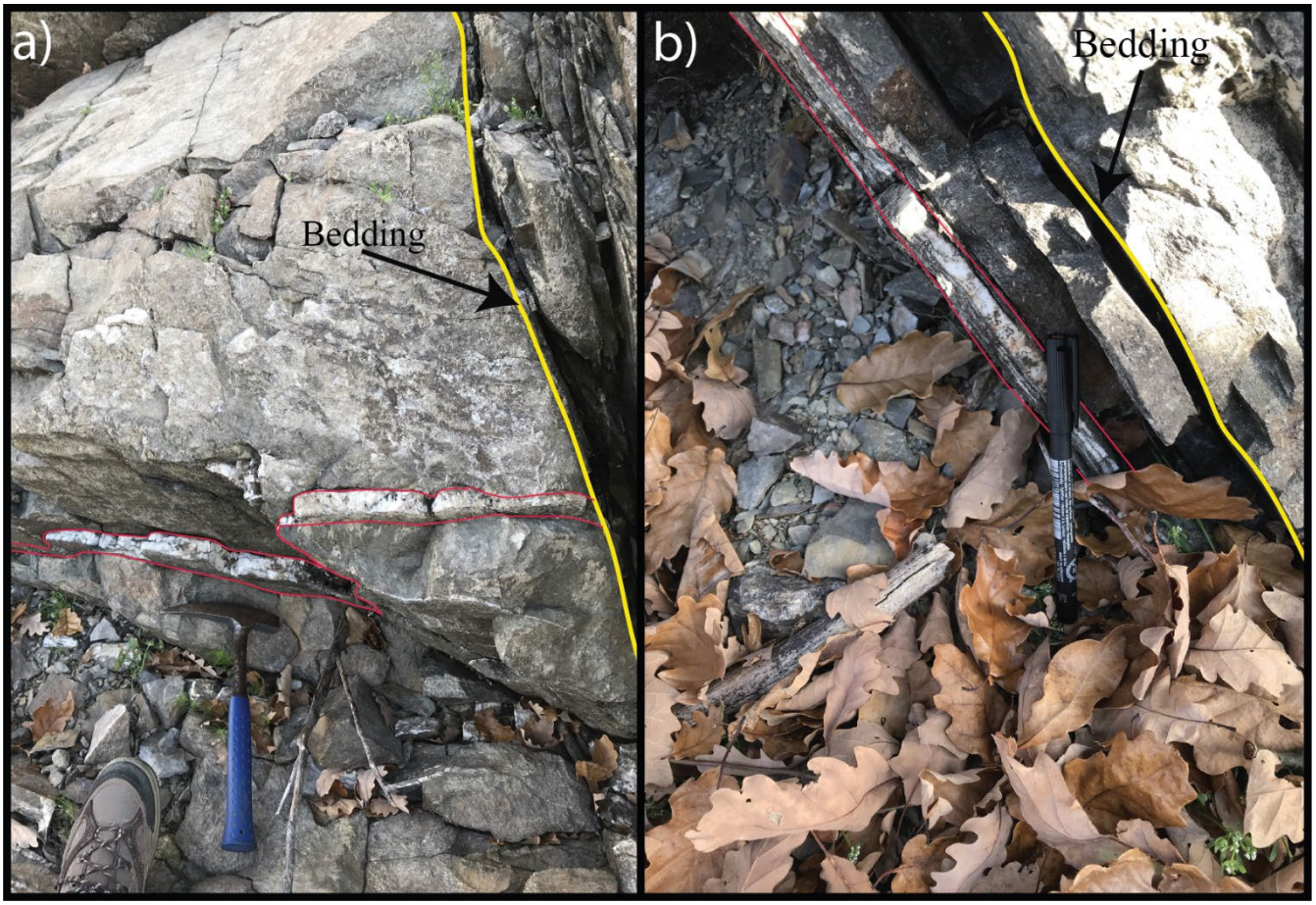

Figure 2: Images of studied outcrop from the Rursee area. The image (a) presents the bedding normal veins (red lines), while (b) shows the bedding parallel veins (red lines). Yellow lines indicate the bedding in both images.

2 Material and methods

2.1 Quartz and inclusions in quartz minerals

A total of seven samples of different veins (3 BNVs and 4 BPVs) were collected from the Rursee outcrop for $^{40}Ar/^{39}Ar$ analysis (Table 1). Both vein types mainly consist of elongated-fibrous milky quartz grains that are characterised by syntaxial growth, whereby the growth starts from the wall of the veins towards the central part of the veins (Ramsay, 1986). The pelitic host rocks consist of sericite, illite, mica and chlorite. Chlorite is also abundant within the vein fractures and between the host rock and the vein wall.

Both quartz vein generations lack of primary fluid inclusions in the crystal growth zones and contain pseudo-secondary and secondary fluid inclusion assemblages (FIAs) (<10 μm) (Van Noten et al., 2011) in the sealed microcracks being perpendicular to crystal elongation (Fig 3.). The Rursee quartz vein samples yield average fluid inclusions homogenization temperatures (minimum trapping temperature, T_h) of ~135 ±25 °C and ~160 ±20 °C for BPV and BNV, respectively, with salinities of 3.5-8 eq. wt.% NaCl In general, T_h of pseudo-secondary and secondary fluid inclusions span an equally broad range of 110-180 °C (Van Noten et al., 2011).

2.2 Mineral separation

Prior to $^{40}Ar/^{39}Ar$ analysis, mineral separation was conducted at Vrije Universiteit Amsterdam (VU; The Netherlands). The bulk vein samples were crushed, washed, and cleaned in an ultrasonic bath for at least one hour to remove the adhering host rock contaminants from quartz grains. The samples were sieved into 250 and 500 μm fraction and dried in an oven at 60 °C. The samples were further separated by a custom-made system using an overflow centrifuge with conventional heavy liquids based on IJlst (1973) and Frantz magnetic separation (Porat, 2006). We used heavy liquids with a density of 2.62 g/cm^3 and 2.64 g/cm^3 to obtain fluid inclusion-rich fraction of quartz grains (ρ= 2.62-2.64 g/cm^3). The fraction was rinsed with acetone, dried, and further sieved to separate the 400-500 μm grain size range. From this fraction, only the purest quartz grains were hand-picked under binocular microscope for $^{40}Ar/^{39}Ar$ dating.

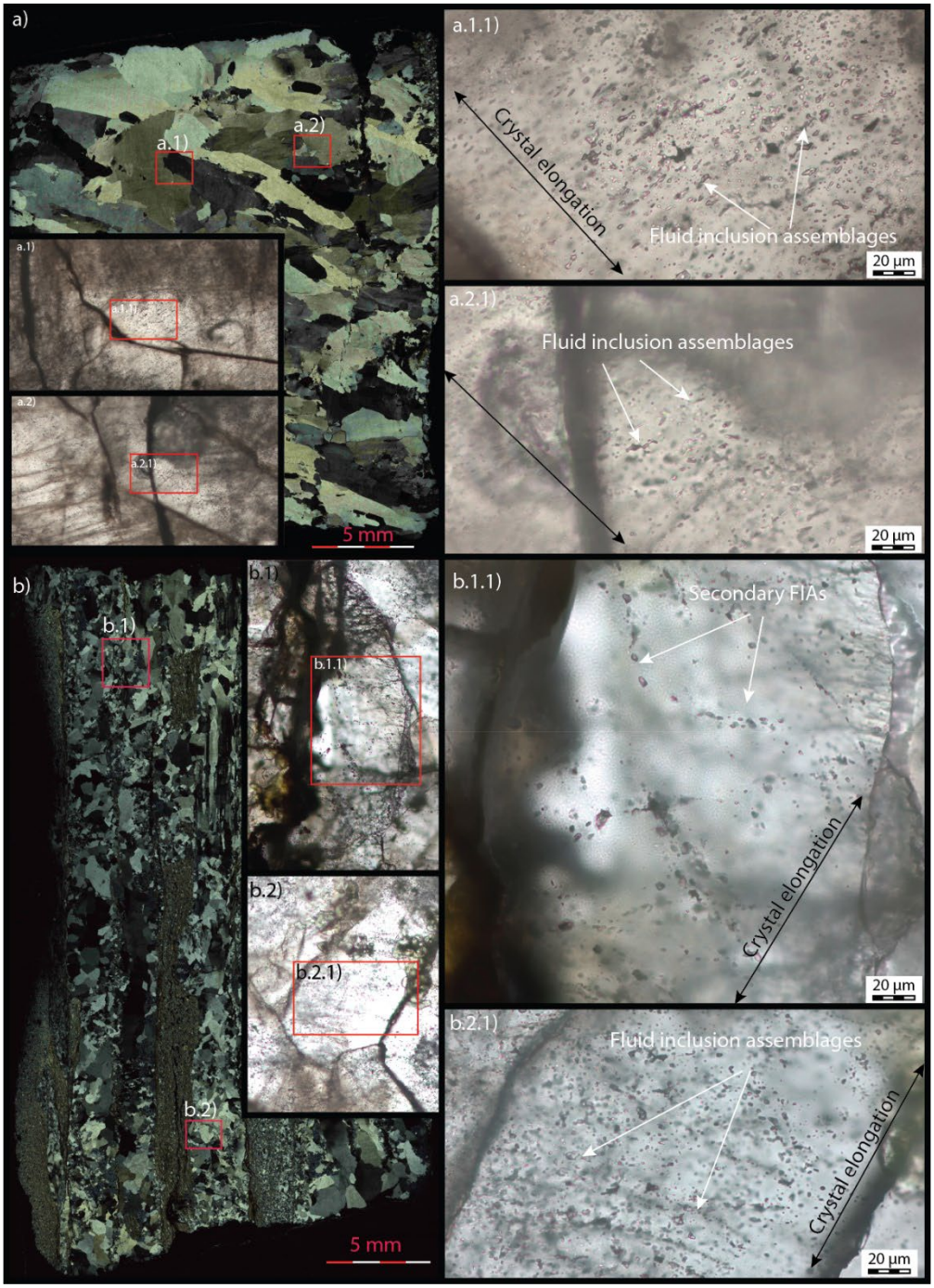

Figure 3: Fluid inclusions in quartz veins under optical microscopy. (a) Image of BNVs under cross-polarizer light microscopy. Both (a.1.1) and (a.2.1) are the zoom of (a.1) and (a.2) images, respectively, indicating pseudo-secondary fluid inclusion assemblages (FIAs) (white arrow). (b) Cross polarizer images of the BPV sample under microscopy. (b.1.1) and (b.2.1) images are secondary and pseudo-secondary fluid inclusion (respectively) -focused areas, which are zooms of the (b.1) and (b.2) images, respectively. The white arrows represent the FIAs. Both generations of quartz veins have FIAs that are present in sealed microcracks rather than in crystal growth zones.

2.3 $^{40}Ar/^{39}Ar$ stepwise crushing

Fluid-rich quartz grains (400-500 µm; 2.62-2.64 g/cm^3) were carefully selected under a binocular zoom microscope, and a quantity of 200-270 mg of material was packed in aluminium foil and placed in 20 mm ID - 22mm OD aluminium cups. Drachenfels (DRA-2) sanidine standard was loaded between each set of three samples to monitor the neutron flux. The samples were irradiated at Oregon State University (USA) using the CLICIT (Cadmium-Lined In-Core Irradiation Tube) facility for 12 hours (batch VU123). After irradiation, standards were placed in 2 mm copper planchet holes for single grain fusion analysis and vacuum pre-baked at 250 °C. The samples were then placed in an ultra-high vacuum system, baked at 120 °C, and connected with hot NP10 and ST172 getters, Ti getter sponge at 400 °C, and a cold trap at -70 °C. The standards were fused with a Synrad 48–5 CO_2 continuous-wave laser fusion system.

The samples were crushed in an in-house developed and built crusher consisting of a stainless-steel tube (height: 18 cm, outer diameter: 1.8 cm) that has a spherical curve on its interior base and a magnetic stainless-steel pestle (height: 5 cm, diameter: 1.6 cm, weight: ~69.5 g) with rounded tips with a slightly narrower outer radius. These geometries allow optimisation of the impact on the sample while crushing. Once a split of the sample (~30 mg of quartz grains) was loaded into the crusher tube, the pestle was carefully relocated to the bottom of the tube to avoid crushing the sample. The crush tube, the pestle, and the sample were baked overnight at 250 °C. The pestle was dropped into a free-fall state using an external electromagnet with a frequency of 1 Hz controlled by an adjustable power supply and pulse generator to crush the sample. The pestle was dropped from a height of ~3, ~4 or ~5 cm *in vacuo*. Subsequently, the gases emitted from fluid inclusions in the fragmented quartz sample were analysed. To obtain a sufficient amount of argon in the mass spectrometer, the number of pestle drops per extraction step and drop height were systematically increased during the experiment, with a maximum of 999 drops per analysis (in total, ~40000 cumulated pestle drops per experiment).

The gas released from the samples and standards was analysed isotopically using a ThermoFisher Scientific Helix MC+ mass spectrometer. The Helix MC+ mass spectrometer is a 5 collector channel instrument, equipped with a total of 10 collectors, a Faraday collector optionally fitted with a 10^{12} Ohm or 10^{13} Ohm resistor amplifier and a compact discrete dynode secondary electron multiplier (CDD-SEM) collector on each collector channel. Five collectors can be used at the same time to simultaneously collect the beam intensity signals of the 5 isotopes of argon. The H2-Faraday collector is employed for the detection of ^{40}Ar using a 10^{13} Ohm amplifier. Similarly, the H1- CDD collector is used for the measurement of ^{39}Ar (H1 Faraday was used for the runs on DRA-2 sanidine standard because of the higher ^{39}Ar signal), the AX-CDD collector for ^{38}Ar, the L1-CDD collector for ^{37}Ar, and the L2-CDD collector for ^{36}Ar.

Line blanks were measured after every three to four unknowns and subtracted from the succeeding sample data. A Gain calibration is done by correcting for gain relative to the beam intensity measured on the AX-CDD, using measurements of ~50 fA (^{40}Ar measured beam intensities) pipettes of air on each cup, and mass discrimination corrections are made by measuring a series of ~400 fA (^{40}Ar measured beam intensities) air pipettes roughly every 12 hours. Raw data were processed using the ArArCalc software (Koppers, 2002). Ages are calculated relative to Drachenfels (DRA-2) sanidine of 25.552 ± 0.078 Ma

(Wijbrans et al., 1995) which was recalibrated against Fish Canyon Tuff sanidine of 28.201 ± 0.023 Ma (Kuiper et al., 2008). The decay constants of Min et al. (2000) are used. The atmospheric $^{40}Ar/^{36}Ar$ ratio of 298.56 ± 0.31 is based on Lee et al. (2006). The correction factors for neutron interference reactions are (2.64 ± 0.02) $x10^{-4}$ for $(^{36}Ar/^{37}Ar)_{Ca}$, (6.73 ± 0.04) $x10^{-4}$ for $(^{39}Ar/^{37}Ar)_{Ca}$, (1.21 ± 0.003) $x10^{-2}$ for $(^{38}Ar/^{39}Ar)_{K}$, and (8.6 ± 0.7) $x10^{-4}$ for $(^{40}Ar/^{39}Ar)_{K}$. Gain correction factors and their standard errors (±1SE) are 1.00162 ± 0.00028 for H2-Far, 0.97963 ± 0.00021 for H1-CDD, 0.99921 ± 0.00027 for L1-CDD and 0.96163 ± 0.00064 for L2-CDD for data measured in 2022 (R2.1) and 1.00465 ± 0.00031 for H2-Far, 0.97033 ± 0.00027 for H1-CDD, 0.99824 ± 0.00033 for L1-CDD, and 0.96309 ± 0.00070 for L2-CDD for data measured in 2023 (R1-R6). The K/Cl ratios are calculated by $K/Cl = \beta \times {}^{39}Ar/^{38}Ar$ with $\beta = 0.06$ derived from K/Cl = ~18.7 in GA1550 and $^{39}Ar_K/^{38}Ar_{Cl}$ = ~316 for a 12-hour irradiation at the OSU Triga CLICIT facility. All errors are quoted at the 2σ level and include all analytical uncertainties (Table 1).

Note that it is not possible to directly correct the crushing blank because we cannot perform the exact experiment without crushing sample material. We tested the blanks for each tube without sample material, following the identical procedures used for real experiments. With this approach, we have direct metal-to-metal contact during pestle drops, which might not be fully representative of a real sample. We did observe a substantial increase in background, with a higher number of drops and a higher drop level. Importantly, the composition of this blank is similar to that of atmospheric argon. Therefore, we follow the approach that the ^{40}Ar signal derived from the line blank (measured every 3-4 unknows where we mimic the sample experiment, but without the crushing / pestle drops) is subtracted from the measured ^{40}Ar intensity. The real blank has an atmospheric $^{40}Ar/^{36}Ar$ ratio and is incorporated in the air corrections, leading to a lower radiogenic $^{40}Ar^{*}$ if the real blanks are relatively high.

2.4 Electron Probe Microanalysis (EPMA)

Quartz grains of sub-samples that were analysed for $^{40}Ar/^{39}Ar$ were mounted in epoxy resin and carbon coated for the JEOL JXA-8530F hyperprobe field emission electron probe microanalyzer (EPMA) at Utrecht Universiteit (UU; The Netherlands) to define the elemental compositions of 1) the host quartz, 2) minerals that are present in fluid inclusions, filled cavities, or fractures, and 3) mineral inclusions in the quartz. For this analysis, an accelerating voltage of 15 kV and a beam current of 8 nA for host rock (quartz) and 7 nA for mineral inclusions are used with beam sizes of 10 µm and 1 µm, respectively. The elements analysed are Si, Ti, Al, Fe, Mn, Ca, Na, K, P, Cl, F, Ba, and Zr. The data are calibrated using Icelandic rhyolite glass (ATHO-G) and basalt glass (KL2-G) standards that were both measured with a beam size of 10 µm, and multiple times before and after measurements of the samples.

3 Results

The age spectra of the *in vacuo* stepwise crushing of the quartz samples are plotted in Figure 4. All samples show typical release patterns with unrealistically old apparent ages (>6 Ga) in the initial 10 % of $^{39}Ar_K$ released. Note that samples Rursee 1a BNV and Rursee 1b BNV are measured in two different experiments on subsets from the same irradiated sample, yielding different results. For sample Rursee 1a BNV, a lighter pestle (68 g) has been used than for sample Rursee 1b BNV (69.5 g) and for all other samples.

The apparent ages of the spectra in samples Rursee 1b BNV, Rursee 2 BPV, Rursee 2.1 BNV, and Rursee 4 BPV exhibit a gradual decrease in age over the next 10 - 40 % of $^{39}Ar_K$ released, eventually stabilising at a more or less consistent maximum apparent age from ~80 to ~100 % $^{39}Ar_K$. Rursee 3 BPV, Rursee 5 BNV, and Rursee 6 BPV show comparable behaviour with, after the initial old apparent ages, a decrease in a maximum apparent age to an "early converging section" from ~15 % to ~40 % $^{39}Ar_K$ released, followed by a gradual decrease in apparent age and a more or less uniform apparent age in the >80 % released $^{39}Ar_K$ part of the spectrum. For these early converging sections, we arrive at averaged maximum apparent ages of ~84 Ma for Rursee 1b BNV, ~97 Ma for Rursee 2 BPV, ~117 Ma for Rursee 4 BPV, ~216 Ma for Rursee 2.1 BNV, ~190-200 Ma for Rursee 5 BNV, and Rursee 6 BPV, and ~560 Ma for Rursee 3 BPV. The maximum apparent ages of Rursee 2.1 BNV and Rursee 4 BPV correspond to the inverse isochron maximum apparent ages; however, due to significant uncertainty, the maximum apparent ages of other samples obtained from the average late converging section age (Table 1).

The inverse isochrons (Fig. 5) confirm that the first part of all experiments is heavily affected by excess argon ($^{36}Ar/^{40}Ar$ ratios are much lower than atmospheric composition), followed by an increase in $^{36}Ar/^{40}Ar$ and $^{39}Ar/^{40}Ar$ ratios and clustering of data points on the reference line. The maximum apparent ages that we derive are based on the data points that cluster along the reference line in the isochrons in the final part of the age spectra. There is no systematic maximum apparent age difference between BNV and BPV.

All quartz samples release argon during *in vacuo* stepwise crushing with different isotopes of argon contributing to the gas release at different stages of the experiment. Figure 6 shows, for each step, the percentage (relative to total amount) of a specific isotope that is released through the experiment. All quartz samples are characterised by a release of most of the $^{36}Ar_{air}$ in the first 20 steps. $^{40}Ar^*$ and $^{38}Ar_{Cl}$ follow the pattern of $^{36}Ar_{air}$. The $^{39}Ar_K$ generally starts to increase after the first 20 analysing steps (~790 pestle drops from 3 cm height). At steps 30-35, we observe fluctuations in the data. These shifts are artefacts caused by increasing the drop height (from 3 to 4 cm at ~step 30 and from 4 to 5 cm at ~step 35) and adjusting the number of pestle drops. To prevent high signals, we started with a relatively low number of pestle drops at a higher drop height, yielding low signals, as observed as two troughs at ~step 30 and ~step 35 in all experiments. All quartz samples are low in $^{36}Ar_{air}$, $^{38}Ar_{Cl}$, and ^{40}Ar* at the end of analysis compared to their total release. For $^{40}Ar^*$, we still measure a small, reliable signal, but this is obscured in Figure 6 due to the high signals in the first steps since we plot percentages of the total released ^{40}Ar per experiment. Note that huge amounts of excess ^{40}Ar (which is part of the $^{40}Ar^*$ signal) are released in the initial steps of the experiment and dominate the total percentage.

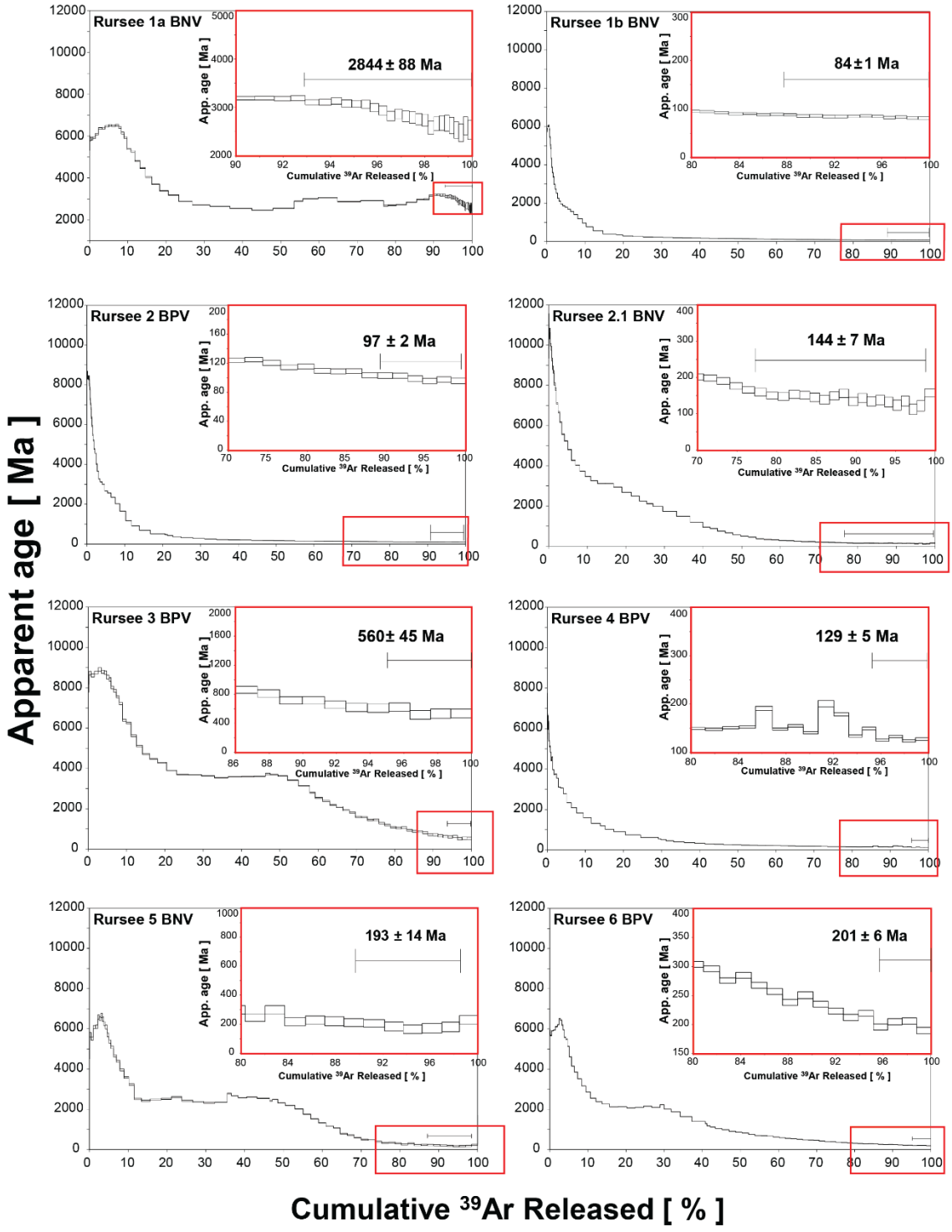

Figure 4: The apparent "late converging section" age of all quartz vein experiments. The red boxes focus on the last part of the age spectra, where apparent ages are more or less stable.

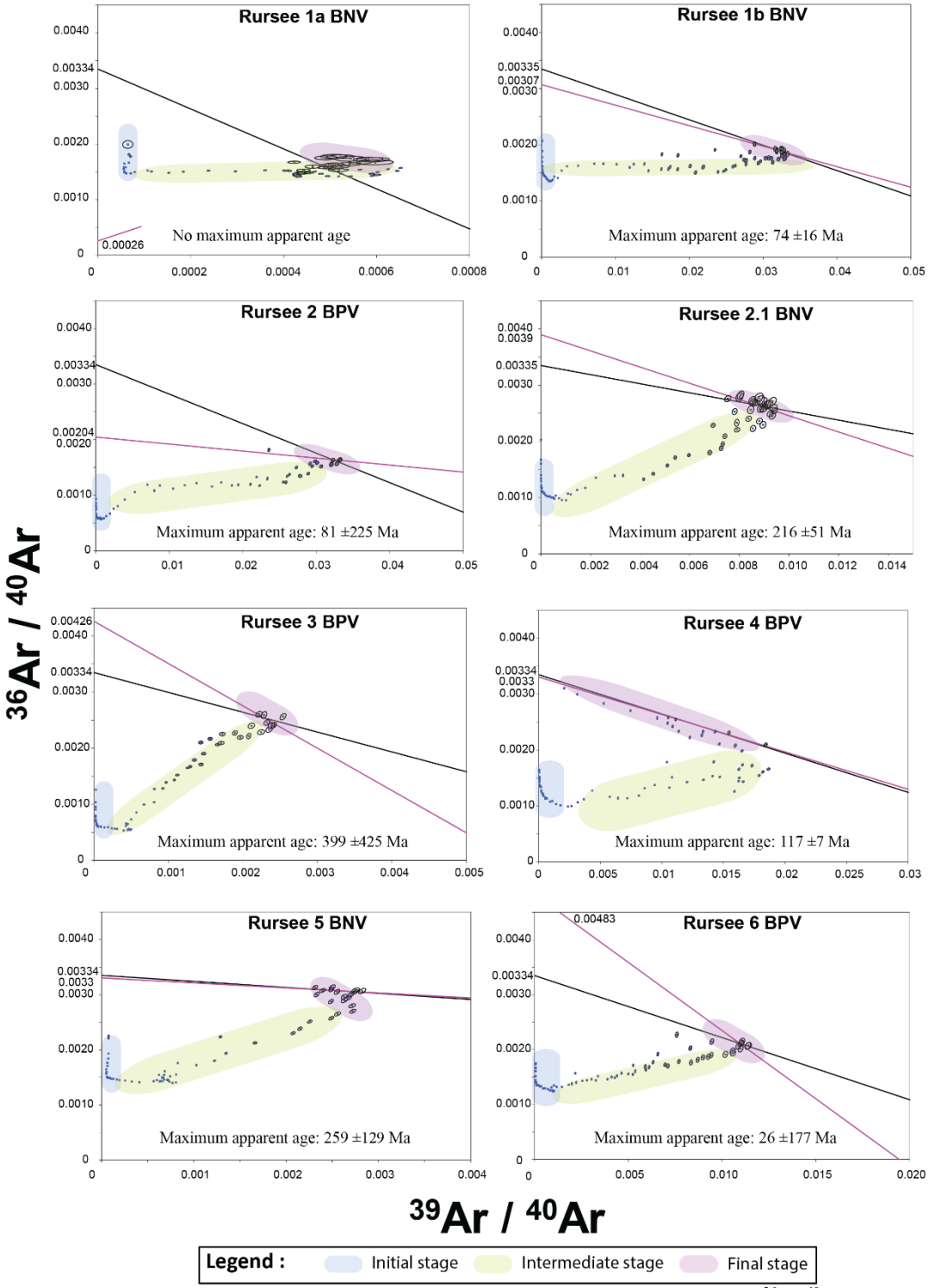

235 **Figure 5: Inverse isochrons of all quartz veins samples. Dark line corresponds to the atmospheric $^{36}Ar/^{40}Ar$, while pink line shows**
236 **mean weighted.**

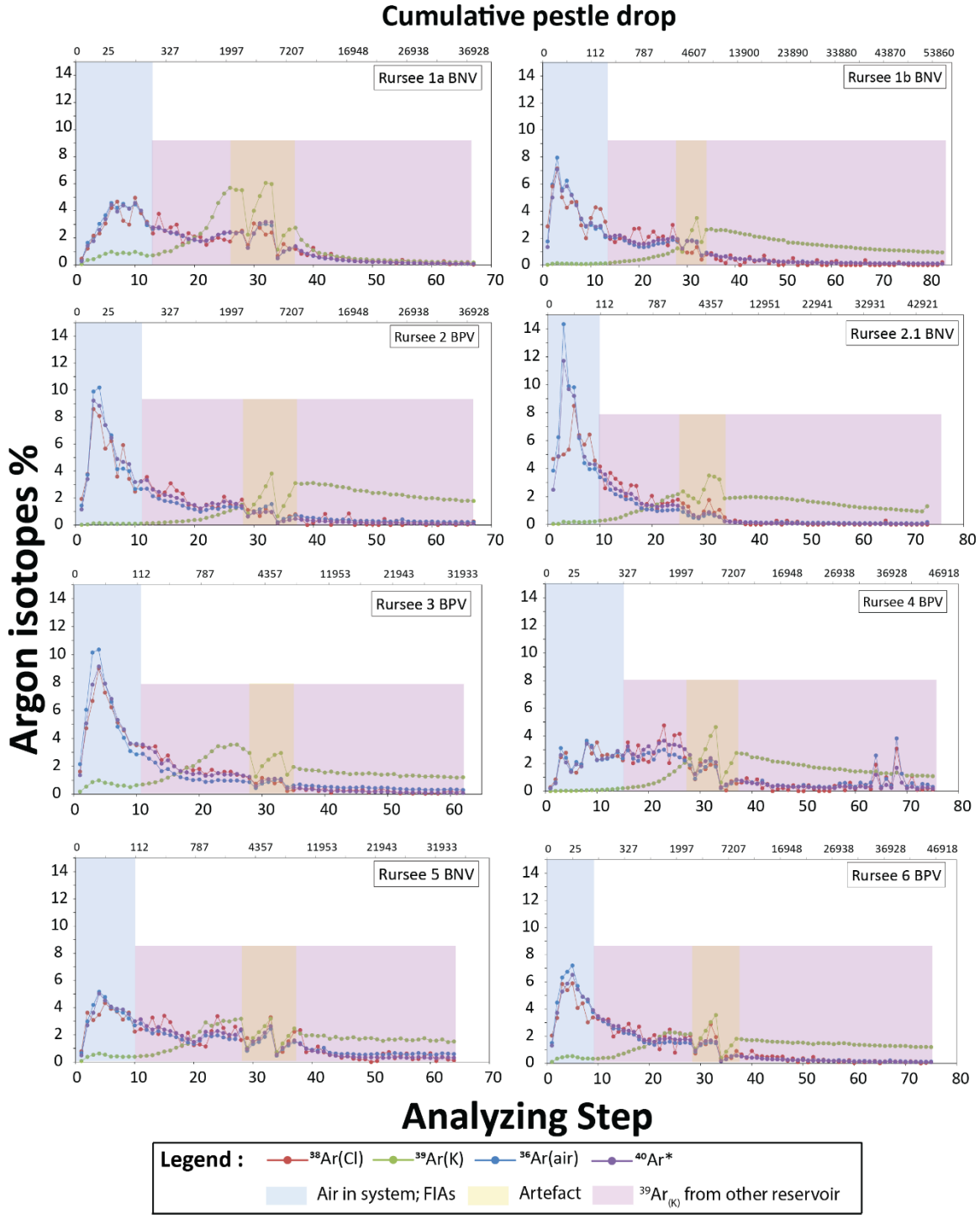

237 **Figure 6: Released argon isotopes per analysing step relative to its total release. Note that the data are expressed against analysing**
238 **step instead of the crushing step, and that the upper x-axis scaling (cumulative pestle drops) are neither linear, nor logarithmic (non-**
239 **continuous scaling).**

240 **Table 1 Summary of $^{40}Ar/^{39}Ar$ age spectra, including invers isochron data of all analysed quartz samples. The maximum apparent**
241 **ages of late converging section and inverse isochron selected, as discussed in the text, are highlighted in bold, with an asterisk**
242 **marking those used for geological interpretation.**

Locality	**Rursee, outcrop near Schwammenauel dam (Germany)**							
Rock type	Quartz veins							
Mineral	Quartz							
Sample ID	**Rursee 1a BNV**	**Rursee 1b BNV**	**Rursee 2 BPV**	**Rursee 2.1 BNV**	**Rursee 3 BPV**	**Rursee 4 BPV**	**Rursee 5 BNV**	**Rursee 6 BPV**
Sample ID Ar	R01a	R01b	R02	R021	R03	R04	R05	R06
GPS coordinate	Lat.: 50.63378406 Long.: 6.44191402		Lat.: 50.63377933 Long.: 6.44190753	Lat.: 50.63388498 Long.: 6.44184657	Lat.: 50.63418108 Long.:6.44176707	Lat.: 50.6344143 Long.: 6.4418217	Lat.: 50.63367794 Long.: 6.44201891	Lat.: 50.63392217 Long.: 6.44181953
Grain Size (µm)	400 – 500							
Density (g.cm^{-3})	2.62 - 2.64							
Max. apparent age (Ma)	2844	**84***	**97***	145	**560**	129	**193**	**201**
±2σ analytical error + J error	± 88	± 1	± 2	± 7	± 45	± 5	± 14	± 6
±2σ full external error	± 96	± 2	± 3	±8	± 47	± 6	± 15	± 7
MSWD (app.age)	42.8	1.6	3.3	4.3	6.1	5.4	2	0.4
K/Ca	0.32	1.54	14.28	5.33	0.285	3.21	0.75	3.48
$^{40}Ar/^{36}Ar$ inverse isochrone intercept	3874	326	858	258	329	311	289	243
±2σ analytical error + J error	± 7285	± 51	± 860	± 38	± 183	± 6	± 29	± 181
Inverse isochrone age	-	74	81	**216**	399	**117***	259	26
±2σ analytical error + J error	± 5770	± 16	± 225	± 51	± 425	± 7	± 129	± 177
±2σ full external error	± 5770	± 16	± 225	± 51	± 425	± 8	± 129	± 177
n/n_{tot} (n: number of analyses included weighted mean, n_{tot}: total number of analysis)	22 / 67	11 / 83	4 / 67	19 / 73	4 / 62	4 / 75	9 / 64	3 / 75
MSWD (iso. age)	14.5	1.6	0.2	3.8	8.8	0.9	2.2	0.5

4 Discussion

During *in vacuo* stepwise crushing, the release of argon isotopes from the samples follows systematic patterns. The challenge is to link this release of argon from the samples to the different potential reservoirs of K and, as a next step, the geological meaning of the age and elemental ratios of K/Cl and Ca/Cl. Here, we first discuss potential issues related to the analytical quality of the data. Next, we discuss potential reservoirs of K and subsequently $^{40}Ar^{*}$ to link these options to our results, and to finally assess the maximum apparent ages and their broader implications.

4.1 Data quality

4.1.1 Rursee 1a/1b BNV

We speculate that for the experiment Rursee 1a BNV, we sampled a smaller part of the argon reservoirs in the quartz minerals comparable to the first 10 % of the spectrum of Rursee 1b BNV. This is corroborated by the fact that for Rursee 1a BNV, 46 mg of quartz released 12.7 fA $^{39}Ar_K$ (0.3 fA/mg quartz), while for Rursee 1b BNV, 89.1 fA was released from 25 mg of quartz (3.6 fA/mg of quartz). We therefore do not further discuss the results of Rursee 1a BNV, but note that sample heterogeneity might also have contributed to this difference.

4.1.2 Impact of blank correction

Blank correction procedure likely does not impact weighted mean age computation; however, it does influence the $^{40}Ar/^{36}Ar$ intercept of the inverse isochron. This is only the case when the regression line has a non-radiogenic intercept that is different from the atmospheric $^{36}Ar/^{40}Ar$. When the intercept is within the error overlapping with the atmospheric ratio, the blank correction only causes the point to move along the regression line as comes out of the discussion below as well. We described our blank correction procedure in methods (see supplementary file 1). The fact that we cannot mimic the dropping of the pestle when a sample is present in the tube provides limitations on how well we can determine the blank during the experiments. The blank tends to increase with higher number of pestle drops, but composition of this blank is atmospheric. For the test of the blank, we used quartz glass fragments to mimic zero-age minerals, as a blank determination using metal on metal impacts was considered to be an unrealistic scenario. As a next test we artificially increase the ^{40}Ar blank (and thus the ^{36}Ar blank) assuming atmospheric composition. If the data are located on the mixing line between radiogenic and atmospheric argon, this should not affect isochron apparent age (pink part – final stage in fig. 5 or 11). We tested this for sample Rursee 1b BNV with an apparent age of ~88 Ma. The $^{40}Ar/^{36}Ar$ intercepts increase with increasing blank values, and the weighted mean late converging section ages change with a maximum of 2.5 Ma in the chosen example. We therefore conclude that the isotopic ages remain largely unaffected, by varying the amounts of atmospheric argon of the blanks. Note, that if the isochron is not a mixing line between radiogenic and atmospheric argon (e.g. blue and green parts in fig 5 or 11), this assumption is incorrect. The $^{40}Ar/^{36}Ar$ intercept is then pulled away from the real $^{40}Ar/^{36}Ar$ composition in the direction of the atmospheric $^{40}Ar/^{36}Ar$ intercept. Consequently, in the intercept with the inverse isochrons' X-axis (and thus age) will also be affected.

4.1.3 Recoil artefacts

These artefacts occur when ^{37}Ar and ^{39}Ar, which are formed from K and Ca isotopes, form with kinetic energy. As a result, they can travel from their original sites to other sites, potentially even into the adjacent phase (Turner & Cadogan, 1974; Foland, 1983; Lo & Onstott, 1989; Féraud & Courtillot, 1994; Baksi, 1994; Onstott et al., 1995; Villa, 1997). However, this phenomenon is assumed to have a smaller impact than that of the blank correction.

4.2 Potential reservoirs of K

To date, three main hypotheses are being debated as to the origin of the released argon in a stepwise crushing experiment. The first group (Qiu & Wijbrans, 2006, 2008; Bai et al., 2019) suggests that progressive crushing releases gases mainly from fluid inclusions and therefore represents fluid inclusions maximum apparent ages. Additionally, the possibility of argon releasing within K-mineral by prolonged crushing when the grain sizes were reduced to tens of nanometres (Bai et al., 2019).

The second group (e.g., Kendrick and Philips (2007)) discusses the possibility of K-bearing mineral inclusions within the inclusion cavity and/or in microcracks serving as argon reservoirs in the later stages of crushing. Obtained maximum apparent ages therefore represent mineral closure ages or a mixture of fluid inclusions and mineral inclusion ages. Accordingly, the gas release sequence under sufficient crushing progresses from microcracks to secondary fluid inclusions, followed by primary fluid inclusions, and finally to micro- to nanometer-sized minerals (Bai et al., 2022).

In addition, the third potential source of potassium in the minerals might be the presence of K^+ in the crystal lattice which was postulated for zeolites (Kendrick et al., 2011), but could also work for feldspars, but may be less of an issue in nominally potassium free minerals such as quartz (or garnet), which is representative of the formation age of veins. Hydrothermal quartz veins, characterised by their substitution in crystal structure, have been studied by Weil (1984) and Götze et al. (2021). These studies indicate that Si^{4+} derived from hydrothermal quartz veins has the ability to be substituted by other ions such as Al^{3+}, Ga^{3+}, Fe^{3+}, B^{3+}, Ge^{4+}, Ti^{4+}, and P^{4+}. Al^{3+} is most commonly replacing Si^{4+} since it is found in significant quantities (~300-700 ppm) in quartz, based on EPMA data. Additionally, small quantities of monovalent ions such as K^+ may fill empty spaces in the crystal structure, serving as charge balancers for trivalent substitutional ions such as Al^{3+} (Bambauer, 1961; Kats, 1962; Perny et al., 1992; Stalder et al., 2017; Potrafke et al., 2019). However, Jourdan et al. (2009) postulated that the substitution of these components may be so minor that it is even undetectable using a Secondary Ion Mass Spectrometer (SIMS). Furthermore, it is important to note that not all hydrothermal sources or quartz minerals have this particular form of substitution (Jourdan et al., 2009).

Apart from these potential $^{39}Ar_K$ reservoirs above, detrital minerals (e.g., mica present in the surrounding pelitic rock) that might be trapped by the quartz veins during the growth may also contribute to the obtained maximum apparent ages.

4.2.1 Identification of different K reservoirs in the Rursee quartz samples

During *in vacuo* stepwise crushing, the release of argon isotopes from the samples follows systematic patterns. Here, we attempt to link this release to the sequential contributions of different reservoirs of K and, thus, argon from the Rursee samples. The release patterns of $^{36}Ar_{air}$, $^{38}Ar_{Cl}$, $^{39}Ar_K$, and $^{40}Ar^*$ (Fig. 6) for all quartz vein samples may originate from multiple existing argon reservoirs.

Depending on the size (<10 µm), location, and generation of fluid inclusions, they may contribute successively to the argon release patterns in the early or middle stage of stepwise crushing. Figure 6 reveals that the concentration of $^{39}Ar_K$ increases throughout the process of *in vacuo* stepwise crushing, while the concentration of other argon isotopes decreases. This suggests that K-containing reservoirs were not opened in the first part of the experiment. The release patterns of $^{39}Ar_K$ can be categorised into two distinct groups during stepwise crushing:

a) The *first group* of samples exhibits a small initial release during the early stages, followed by a decrease in the ~10th step and an increase from the ~10th to ~35th step followed by a gradual decrease (Rursee 3 BPV, Rursee 5 BNV, and Rursee 6 BPV).

b) The *second group*, on the other hand, lacks the initial release of $^{39}Ar_K$ steps 1-10, but behaves the same for step 10 onwards with a gradual increase to the ~35th step followed by a gradual decrease (Rursee 1b BNV, Rursee 2 BPV, Rursee 2.1 BNV, and Rursee 4 BPV).

The continuous rise in $^{39}Ar_K$ levels after ~10 steps in both sample groups, suggests that the gas release process can be divided into at least two phases. Initially, during the first ~10 steps, $^{39}Ar_K$ is emitted from fluid inclusions in microcracks (secondary fluid inclusions). From steps ~10th to ~70th, the release occurs as a result of mixing of potential pseudo-secondary fluid inclusions (~10- ~15th steps), mineral inclusions and/or the crystal lattice of quartz veins. This interpretation is supported by the K/Cl correlation plots (Fig. 7), which show a consistent lower K/Cl ratio until the ~10th step.

From the 10th to the 15th K/Cl ratio, it reaches ~1 with a steep rise for all quartz samples, and later (from ~20th step) this ratio continues to increase steeply for *the second group* of samples, while it shows a less pronounced increase for *the first group* of samples.

The lower K/Cl ratio may be attributed to the presence of Cl and a lack of or limited amounts of K in combination with relatively constant low salinity levels (3.5-8 eq. wt.% NaCl) inside the fluid inclusions, which are likely to be opened in the early phase. After most fluid inclusions have been mechanically opened, the subsequent rapid increase in K (reflected by the $^{39}Ar_K$) and the steady decline in Cl (reflected by the $^{38}Ar_{Cl}$) occur throughout successive crushing steps and is reflected in the K/Cl ratio. Therefore, this increase is most likely caused by the exhaustion of the Cl-rich fluid inclusions in combination with the presence of minerals containing potassium and/or potassium from the crystal lattice of quartz that release their argon in the later crushing steps.

This approach to distinguish between fluid inclusions and other K reservoirs was first suggested by (Kendrick et al., 2006, 2011): K/Cl ratios ≤1 are representative for fluid inclusions and K/Cl ratios >1 for other sources. Therefore, if K/Cl ≤1, the

obtained apparent age corresponds to the maximum apparent age of the fluid inclusions. If the K/Cl >1 the obtained apparent age corresponds to the maximum apparent age of the trapped K-bearing mineral and/or K from the crystal lattice (Kendrick et al., 2006, 2011). In our samples the K/Cl is greater than 1 after the first ~15±3 steps in all quartz vein samples, indicating the presence of major K-related reservoir(s) other than fluid inclusions. It is worth noting that this is based on the assumption that there are no other K-bearing phases, such as KNO_3, K_2SO_4 or K_2CO_3, rather than KCl dissolved in aqueous fluid inclusions. This assumption may be verified by Raman analysis (see Figure A1), which does not show significant peaks for these alternative K-bearing phases. However, the low peaks in ~1080 cm^{-1} may be related to either K_2CO_3 or only noise related to the epoxy background. Therefore, K/Cl >1 suggests that K is either related to the salinity of the fluid inclusions together with different K-components (i.e., KCl and K_2CO_3) or, in case of noise from the epoxy background, at least one major other source should be present, e.g., the crystal lattice of quartz and/or mineral inclusions in the quartz crystals and/or in microcracks.

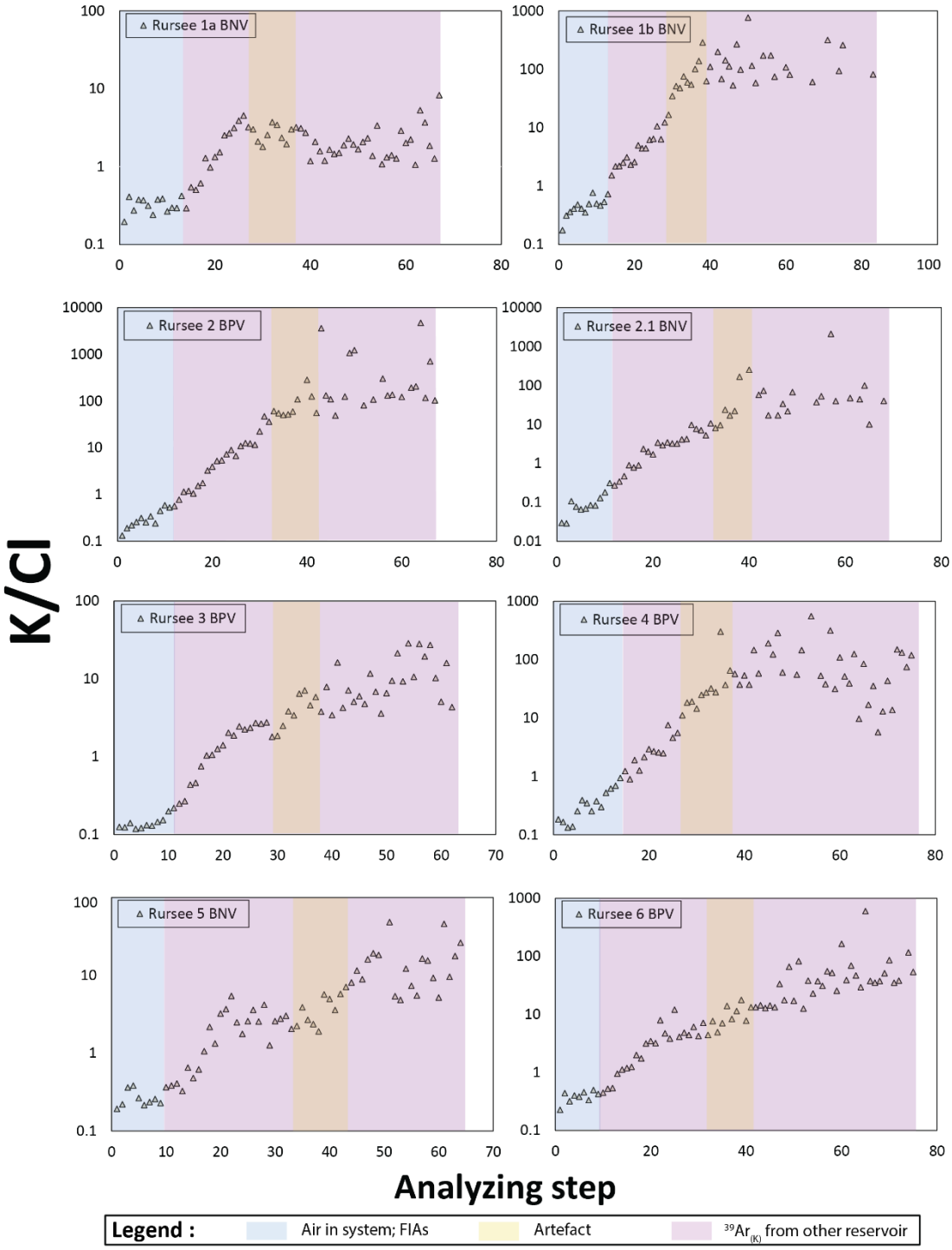

346 **Figure 7: K/Cl ratios plotted against analyzing steps for all quartz veins.**

4.2.2 K-bearing mineral inclusions

EPMA data (Table 2) from cleaned hand-picked fluid-rich separated quartz grains indicate the presence of sericite, chlorite-sericite and illite-sericite in the microfractures and in the cavities of fluid inclusion. The presence of such minerals (or mixtures) in the inclusion cavity and microfractures is also invisible under a binocular or petrographic microscope during the mineral separation, was confirmed captured using electron-backscattered imaging (Fig. 8). In thin sections of quartz veins with associated host rock, illite-sericite and white mica are abundant in the surrounding pelitic layer of the Rursee formation (Fig. 9). These minerals that contain a significant amount of K_2O are also detected by EPMA, in the separated quartz samples, especially in Rursee 2 BPV (see EPMA data, Table 2). High K concentrations (~8.8 wt. % K_2O) are likely related to intergrowth with sericite or a closely-related mineral.

Additionally, petrographic analysis of thin sections of whole rock samples representing both vein generations (BPV and BNV) show an abundance of chlorite in between the vein wall and host rock, as well as in fractures (Fig. 10). Despite the nominal absence of K in the crystal structure of chlorite, traces of K were reported for chlorites in previous studies (Pacey et al., 2020; Li et al., 2022).

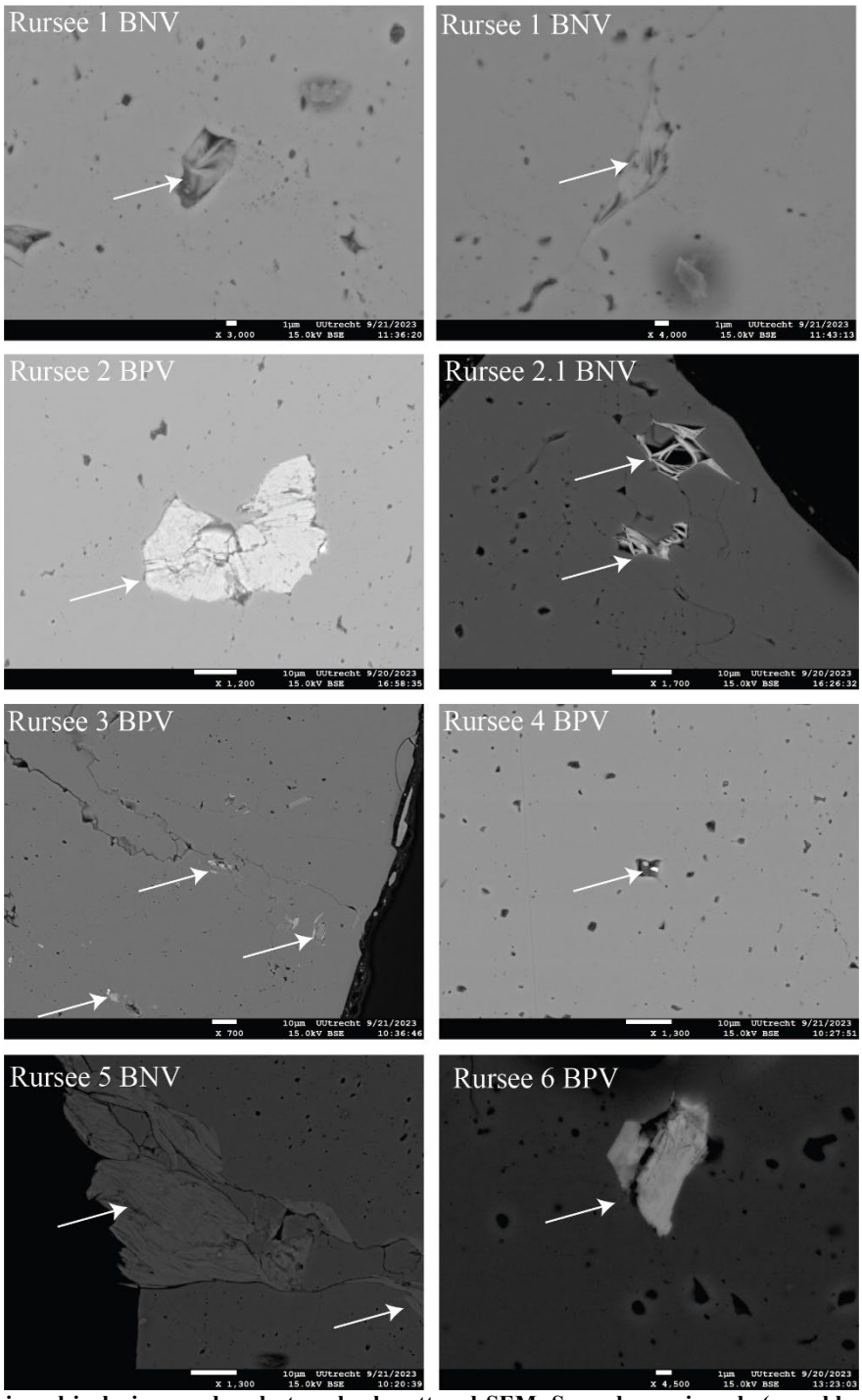

360 **Figure 8: Images of mineral inclusions under electron-backscattered SEM. Secondary minerals (e.g. chlorite, sericite and mica)**
361 **occur in cavities and microfractures (pointed by white arrow) in separated fluid-rich quartz fraction as determined using EPMA.**

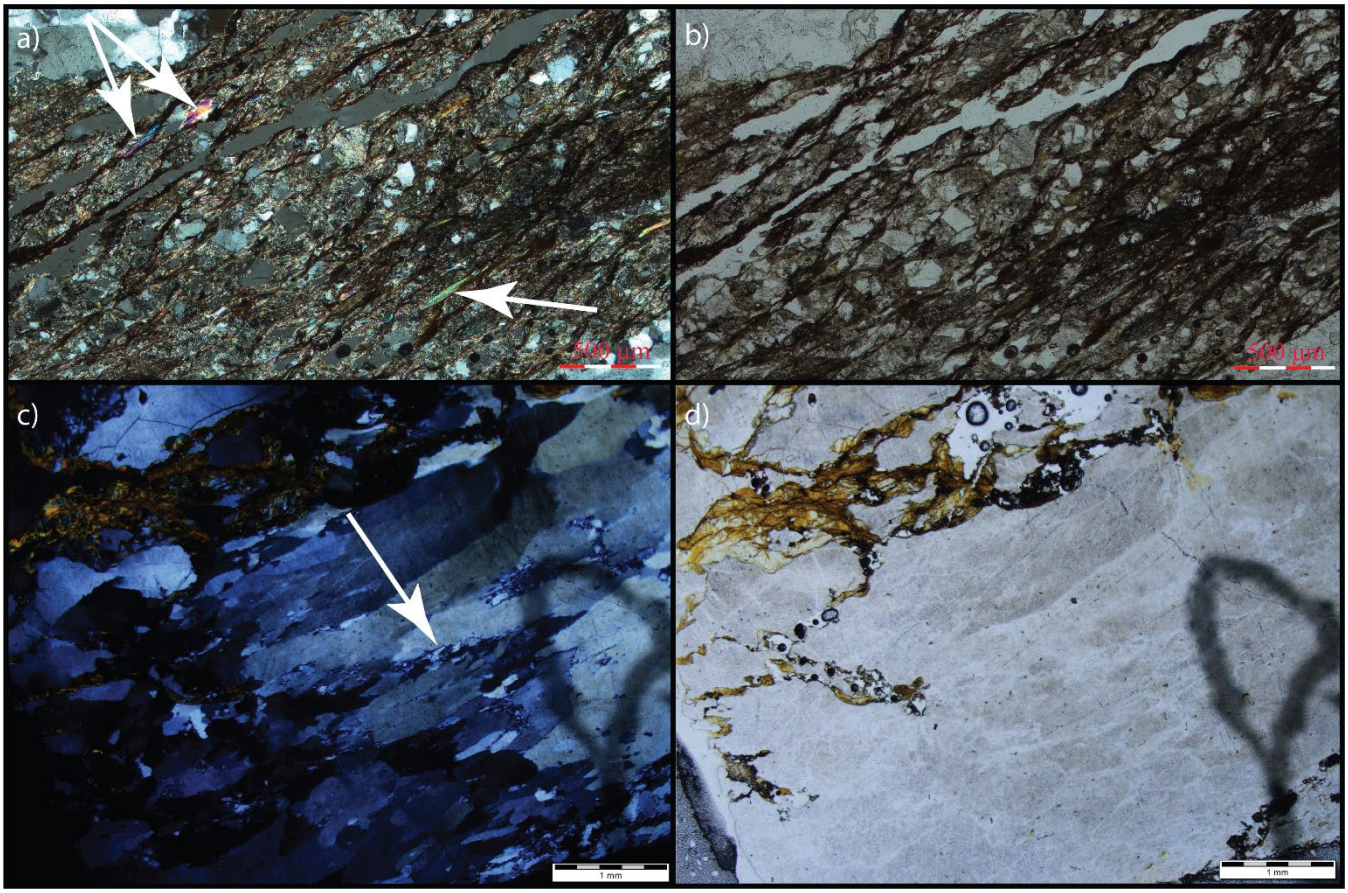

Figure 9: Microscopic image of the quartz veins host rock matrix from the Rursee formation. (a) Cross polarizer (b) plane polarizer images of the pelitic host rock (Rursee 2 BPV). White arrows (image a) indicate the presence of the mica and sericite in the host pelitic rock. (c) Cross polarizer (d) plane polarizer images of the quartz veins matrix (Rursee 1 BNV). White arrow (image c) shows the presence of the quartz sub-grains. The presence of quartz sub-grains in the veins are due to the local tectonic activity, indicating that this period is correspond to tectonic activity.

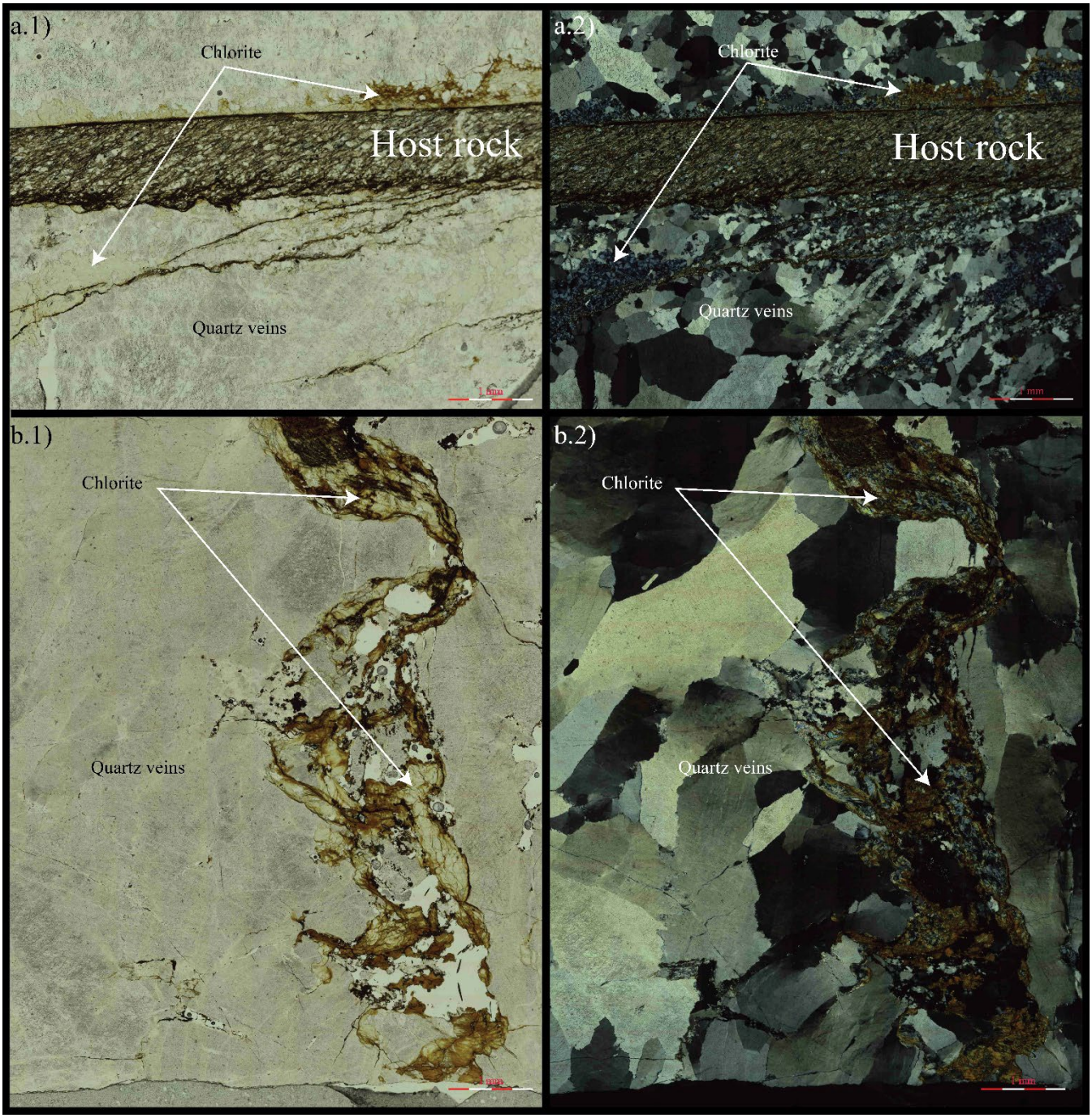

Figure 10: Chloritization distribution in the vein wall and in fractures for both generations of quartz veins. (a) Plane (a.1) and cross (a.2) polarizer of bedding parallel veins: chloritization mainly between vein wall and host rock, and fractures. (b) Plane (b.1) and cross (b.2) polarizer of bedding normal veins: chloritization in fractures.

4.2.3 K from crystal lattice and detrital minerals

EPMA analyses of quartz matrix indicate that K concentrations in the crystal lattice are below the detection limit of ~100 ppm. A maximum K concentration of ~100 ppm K (for example, 100 ppm K in Rursee 2.1 BNV) and a maximum apparent age of 144 Ma would result in ~16000 fA $^{40}Ar^{*}$ when measured on our Helix-MC mass spectrometer, which is a comparable amount of total $^{40}Ar^{*}$ released from K-bearing mineral inclusion. Given the large amount of sample (~30 mg), this would translate into a significant contribution of K from the crystal lattice of quartz. We therefore suggest that K in the crystal lattice may contribute to the observed $^{40}Ar^{*}$ signals (see calculation on supplementary file 2).

In this study, argon molecules might also be derived from secondary minerals in cracks as well as embedded detrital minerals (e.g., mica from host rock). This interpretation aligns with the observation that the homogenization temperatures of fluid inclusions within the quartz veins are below the closure temperature for argon in detrital minerals. Under such conditions, the expected maximum apparent ages from K-bearing detrital minerals would correspond to pre-Variscan periods, reflecting the maximum apparent age of the deposits hosting the quartz veins, while the obtained maximum apparent ages are significantly younger in this study. Therefore, we infer that detrital minerals do not significantly contribute to the $^{40}Ar^{*}$ signals.

To summarise, during the first stages (until the ~20th analysis steps) of the stepwise *vacuo* crushing, gases are likely released only from fluid inclusions (secondary and pseudo-secondary, as is also observed for fluid inclusion in garnets (Qiu & Wijbrans, 2006, 2008)). Huseynov et al. (2024) demonstrated that a significant amount of fluid inclusion water can be extracted from these samples by a single crushing step using a spindle crusher. In this study, throughout the crushing process, the total amount of argon released steadily increases (Fig. 6). In the latter stages of the experiment (from the 20th analysing steps), the substantial release of $^{39}Ar_K$ isotopes may originate as following:

a) The gas release only from the small-sized fluid inclusions (i.e., <5 µm pseudo-secondary) until the last stage of the experiment (~40-50th analysing step) and then in the last stage (after the 50th step) from solid-phase K-bearing minerals and/or crystal lattice, which corresponds to the end of "early converging section" in certain samples. As K/Cl >1 after (the 20th analysing step), the low peak (~1080 cm^{-1}) in Raman spectroscopy may correspond to a K-related component (e.g., K_2CO_3) from fluid inclusions.

b) The significant release of $^{39}Ar_K$ isotopes in the mid- to later stages of the experiment may be related to the presence of non-crushed, small-sized fluid inclusions (<5 µm) together with K-bearing mineral inclusions in the samples and/or $^{40}Ar^{*}$ from the crystal lattice under the condition that low peak in ~1080 cm^{-1} from Raman spectroscopy belongs to the epoxy background of the quartz grain. The contribution of crushing induced degassing K-bearing mineral inclusions is also corroborated by EPMA data, and the presence of K in the lattice cannot be ruled out for the Rursee samples.

4.3 Age spectra and isochrons

As aforementioned, the distribution of argon isotopes (Fig. 6) indicates that $^{39}Ar_K$ is derived from distinct sources, likely mineral inclusions and/or eventually crystal lattice rather than fluid inclusions in particular in the later phase of the experiment,

which was used for the age determinations. These various sources of K, including fluid and mineral inclusions and/or crystal lattice, may all contribute to the variability observed in the age spectra derived from the different samples. Due to the presence of $^{40}Ar_E$ from the fluid inclusions, the initial analytical stages of the analyses yield anomalously high apparent ages in the first part of their age spectra (Fig. 4). Some samples (Rursee 3 BPV, Rursee 5 BNV, and Rursee 6 BPV) show an "early converging section" in the first part of the experiment. The “early converging section” effect occurs between the 20-30th analysing steps, which may be associated with sudden changes in K/Cl ratios (Fig. 7). These sudden changes may be due to sharp transition from fluids states reservoirs (e.g. small sized fluid inclusions) to solid states reservoirs (e.g. K-bearing mineral inclusions). However, it does not occur in *the second group* quartz samples (Rursee 1b BNV, Rursee 2 BPV, Rursee 4 BPV) revealing smooth transitions from fluids to solid states $^{39}Ar_K$ reservoirs. The transition for the Rursee 2.1 BNV is neither abrupt like for the *first group* samples nor smooth as for the *second group* samples; hence, the impact of the “early converging section” is minimal.

The transition from fluid state reservoirs to solid state reservoirs can be supported by grain size distribution (see supplementary file 4), indicating that fluid state reservoirs may remain unreleased beyond around 800 crushes (around the 20th analysis step). However, the accumulation of small particles at the bottom of the crusher (non-recoverable size) after 800 crushes, may result in the measured results not accurately representing the whole grain size distribution. As the grain size distribution depends on many factors (i.e., crushing efficiency, presence of microcracks), even for separated clean quartz grains, that may be a factor of difference for two groups.

The impact of $^{40}Ar_E$ results in inverse isochrons (Fig. 5) during the initial stage. The relationship between the $^{36}Ar/^{40}Ar$ and $^{39}Ar/^{40}Ar$ for all samples resulted in a decrease in the $^{36}Ar/^{40}Ar$ ratio and an increase in the $^{39}Ar/^{40}Ar$ ratio (initial stage in Fig. 11). The presence of an elevated concentration of ^{36}Ar at the beginning of the experiment could be either due to the atmospheric argon gas that is trapped in the stainless steel crusher and/or the original fragment surfaces and perhaps released during the initial stage of crushing. Following the opening of fluid inclusions, the ratio of $^{36}Ar/^{40}Ar$ increases linearly with the ratio of $^{39}Ar/^{40}Ar$. This is probably due to a decrease in excess argon throughout the crushing and an increase in $^{39}Ar_K$ associated with K-bearing minerals and/or crystal lattice (intermediate stage in Fig. 11). In the last phase of $^{40}Ar/^{39}Ar$ analysis, the concentration of $^{39}Ar_K$ decreases (final stage in Fig. 11). This last part is particularly important for determining the age of quartz vein samples.

Inverse isochrons may assist in determining the maximum apparent age of fluid inclusions by linear regression of the data related to fluid inclusions. However, the high amounts of excess argon in the system obscure geologically meaningful ages.

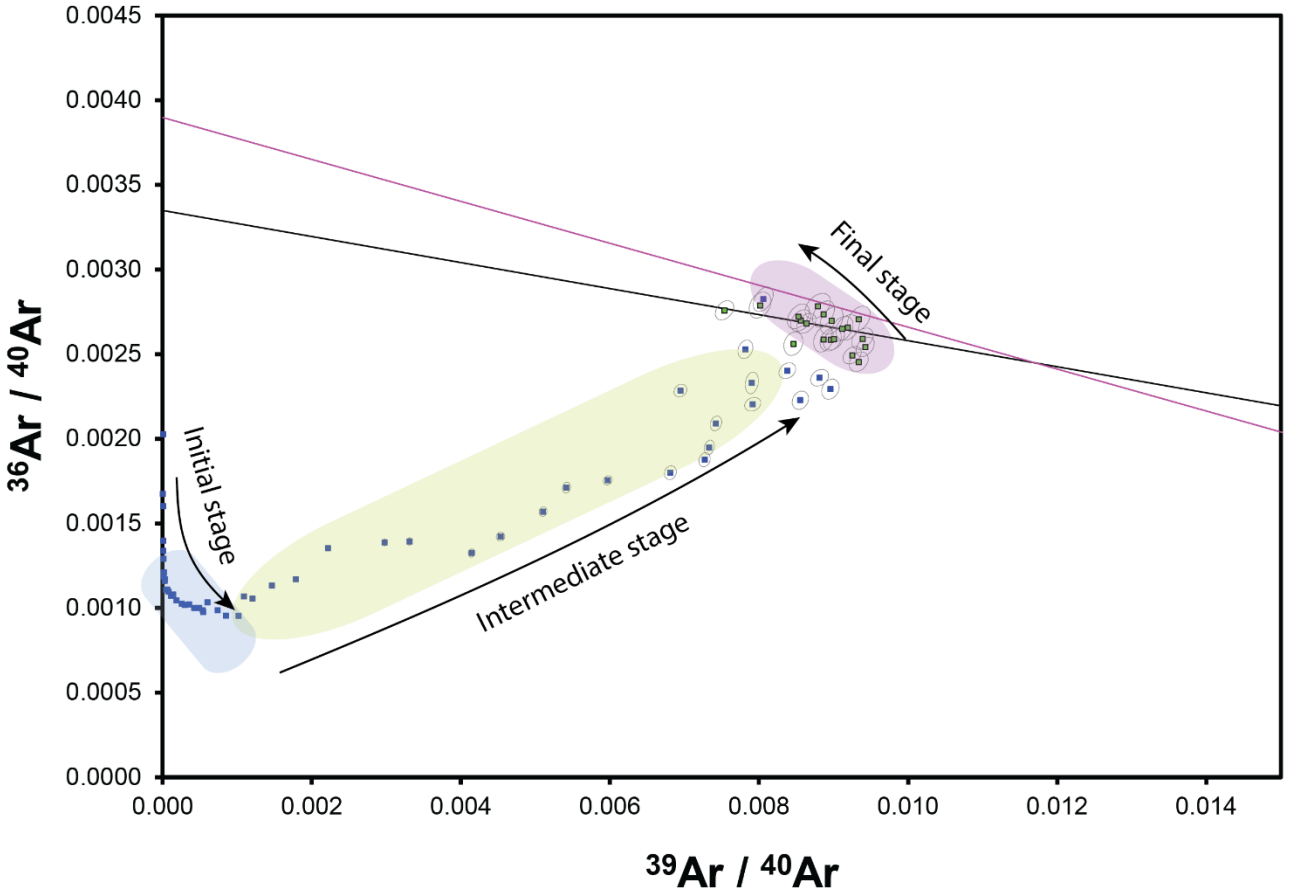

Figure 11: Inverse isochron representation of quartz veins (ex: Rursee 2.1 BNV): 3 stages: (1) initial stage with opening of fluid inclusions; (2) intermediate stage where argon is released from mineral inclusions or microfractures and/or crystal lattice; (3) Final stage of argon release from mineral inclusions and neglectable excess argon in samples.

4.4 Implications

Unlike studies that obtained consistent maximum apparent ages from high salinity (>20 eq. wt.% NaCl) primary fluid inclusions of garnet (in eclogite) and wolframite (Qiu & Wijbrans, 2006; Qiu et al., 2011; Bai et al., 2013, 2019), we were unable to date pseudo-secondary and secondary fluid inclusions in recrystallized Rursee quartz samples, likely due to high $^{40}Ar_E$ concentrations and/or low salinity (3.5-8 eq. wt.% NaCl). The reduced K concentration in the pseudo-secondary and secondary fluid inclusions, due to the loss of the primary brine and its replacement by a lower salinity, lower K fluid, likely led to inaccurate maximum apparent age determination. While no precise age was determined for the fluid inclusions, $^{40}Ar/^{36}Ar$ ratios (above atmospheric but below 4000) indicate a mixed metamorphic-meteoric fluid source (Ballentine et al., 2002; Ozima & Podosek, 2002). Later, during the crushing experiment, the K-bearing mineral inclusions may provide geologically meaningful ages although the argon closure temperatures in quartz remain uncertain. For reference, the closure temperature of smaller size sericite grains (~20 μm) correspond to temperatures (~300-350 °C) (Glasmacher et al., 2001; Watson & Cherniak, 2003), while the vitrinite reflectance from psammatic and pelitic layers indicate maximum burial temperatures (220 ºC) near the Carboniferous-Permian boundary, with gradual cooling thereafter (Littke et al., 2012).

Three $^{40}Ar/^{39}Ar$ maximum apparent ages ranging from 117 to 84 Ma differ from the interpretation based on structural analyses, which posit that veining occurred during the early Variscan Orogeny (Van Noten et al., 2007), possibly due to argon loss during cooling and/or recrystallization. The obtained maximum apparent ages may be influenced to some extent by the presence of neo-crystallized quartz sub-grains, although their volume appears relatively small (Fig. 9c). However, since the maximum apparent ages primarily reflect solid-phase reservoirs (i.e., K-bearing mineral inclusions) rather than fluid-phase components, it is likely that K-bearing solid-phase reservoirs intergrowth simultaneously with the recrystallization process.

Post-Variscan tectonic activity is known for southern Rhenish Massif due to late- and post-orogenic fault movements and coeval reactivation of Variscan structures leading to the fluids (re)activity (Herbst & Muller, 1969; Schwab, 1987; Korsch & Schäfer, 1991; Hein & Behr, 1994; Moe, 2000; Kirnbauer et al., 2012).

Given that reactivation of existing veins could have occurred without forming new fractures (Virgo et al., 2013), this reactivation is usually associated with the infiltration of high saline (>20 eq. wt.% NaCl) fluids in Central Europe and the Rhenish Massif (Behr et al., 1987; Redecke, 1992; Hein & Behr, 1994; Germann & Friedrich, 1999; Heijlen et al., 2001; Kučera et al., 2010).

This saline fluid activity is at odds with the low-salinity fluid inclusions (3.5-8 eq. wt.% NaCl) in the Rursee quartz veins (Van Noten et al., 2011). However they agree with low saline fluid inclusions in quartz veins of the Rhenish Massif, which are attributed to upward migration of Variscan fluid remnants during Jurassic-Cretaceous reactivation (Kirnbauer et al., 2012).

Near Rursee (Stavelot Inlier), low saline (0.2-7.2 eq. wt.% NaCl) and high-temperature fluid activity (~250 °C) along the Variscan front reflect warm meteoric fluid circulation (Schroyen & Muchez, 2000). Such warm, low saline fluids may have also contributed to chloritization of veins in the in Rursee outcrops. We propose that tectonic activity and quartz vein reactivation-recrystallisation could possibly explain the observed $^{40}Ar/^{39}Ar$ maximum apparent ages, as low saline Variscan

466 fluids perhaps moved along the reactivated fractures, forming new quartz minerals within the Variscan-related veins during
467 Jurassic-Cretaceous tectonic activity (i.e. opening of North Atlantic).

468 **Table 2 Elemental analysis of quartz grain, microcracks, and mineral inclusions in quartz vein samples under EPMA.**

EPMA analysis of mineral inclusions and microfractures of clean fraction of quartz veins grain of Rursee samples (wt.%).

	Sample ID	Grain ID	SiO_2	TiO_2	Al_2O_3	FeO	MnO	MgO	CaO	Na_2O	K_2O	P_2O_5	Cl	F	BaO	ZrO_2	O	H2O	TOTAL
Internal standard of UU	KL2-1		51.90	2.56	13.50	10.74	0.17	7.47	10.74	2.39	0.48	0.23	bdl	bdl	bdl	bdl	0.00	0.00	100.01
			51.20	2.51	13.36	10.79	0.17	7.46	10.83	2.38	0.47	0.27	0.00	bdl	bdl	bdl	0.00	0.00	99.28
			50.80	2.55	13.41	10.98	0.16	7.31	10.96	2.34	0.51	0.26	0.00	bdl	bdl	0.00	0.00	0.00	99.13
Internal standard of UU	ATHO-1		75.73	0.21	12.23	3.28	0.11	0.11	1.67	3.85	2.73	0.02	0.05	0.06	0.09	bdl	0.00	0.00	100.10
			75.61	0.24	12.44	3.47	0.12	0.13	1.63	3.73	2.78	0.05	0.05	0.03	0.00	0.02	0.00	0.00	100.29
			75.69	0.28	12.30	3.43	0.12	0.11	1.60	3.78	2.81	0.02	0.03	0.04	0.04	0.10	0.00	0.00	100.35
Rursee quartz veins	Rursee 1 BNV	B_1.01a	99.75	0.02	0.00	0.00	0.00	bdl	0.01	0.02	1.00	0.01	0.59	bdl	bdl	bdl	0.00	0.00	101.21
		B_1.02a	55.07	bdl	0.31	0.29	0.01	0.61	0.88	0.39	0.51	0.13	0.40	bdl	0.03	0.01	0.00	0.00	58.57
		B_1.03a	71.35	0.02	0.69	2.83	0.07	14.04	0.15	0.38	0.51	0.05	0.12	bdl	bdl	0.00	0.00	0.00	90.05
		B_1.03b	38.76	0.04	2.80	1.85	0.02	6.30	0.74	1.53	0.95	0.13	0.30	bdl	0.04	bdl	0.00	0.00	53.29
		B_1.06a	47.68	0.01	37.73	0.04	bdl	0.04	0.19	5.61	0.86	0.05	0.06	0.04	bdl	bdl	0.00	0.00	92.27
		B_1.06b	99.52	bdl	0.67	0.01	0.01	0.00	0.05	0.04	0.04	0.05	0.00	0.00	0.02	0.05	0.00	0.00	100.45
		B_1.06c	92.43	0.02	5.79	bdl	bdl	0.04	0.05	1.01	0.28	0.01	0.03	bdl	0.05	bdl	0.00	0.00	99.60
		B_1.06d	50.05	0.03	25.07	0.01	0.02	0.10	0.08	2.44	3.24	0.05	0.03	0.02	0.00	bdl	0.00	0.00	81.10
		B_1.10a	50.90	0.03	33.68	0.13	bdl	0.13	0.05	1.66	6.22	0.00	0.12	0.04	0.04	bdl	0.00	0.00	92.98
		B_1.11a	52.33	bdl	31.93	0.09	0.00	0.08	0.07	0.29	8.08	0.07	0.03	0.02	0.15	bdl	0.00	0.00	93.00
		B_1.15a	68.06	0.02	24.01	0.00	0.00	0.10	0.39	3.14	0.93	bdl	0.13	bdl	0.03	0.03	0.00	0.00	96.82
	Rursee 2 BPV	B_2.02a	78.24	bdl	0.25	0.32	0.00	0.04	0.37	0.22	0.03	0.19	0.05	bdl	0.05	0.03	0.00	0.00	79.76
		B_2.02b	13.65	0.03	1.51	59.78	bdl	0.31	0.37	1.52	0.95	0.16	0.61	0.02	bdl	0.04	0.00	0.00	78.90
		B_2.03a	47.72	0.07	6.23	5.85	0.15	5.35	3.09	1.64	0.40	0.05	0.20	0.04	bdl	0.01	0.00	0.00	70.79
		B_2.03b	55.38	0.58	2.11	12.35	0.34	9.12	12.46	0.64	0.24	0.02	0.07	bdl	0.04	bdl	0.00	0.00	93.29
		B_2.03c	35.63	bdl	0.79	37.24	0.15	0.22	1.06	1.02	0.56	0.12	0.25	0.00	bdl	0.01	0.00	0.00	77.02
		B_2.04a	24.10	0.01	22.59	30.81	0.18	7.20	0.03	0.04	0.03	0.05	0.01	0.00	0.03	0.01	0.00	0.00	85.09
		B_2.05a	24.15	0.04	22.79	31.10	0.15	8.04	bdl	0.01	bdl	0.00	0.00	bdl	bdl	bdl	0.00	0.00	86.14
		B_2.09a	23.19	0.04	23.09	33.29	0.20	7.22	0.03	0.01	0.03	0.00	0.02	0.02	0.00	0.01	0.00	11.05	98.18
		B_2.09b	47.70	0.05	35.29	0.83	0.02	0.88	0.01	0.28	8.78	0.00	0.02	0.13	0.13	bdl	0.00	4.59	98.70
		B_2.12a	100.15	bdl	0.06	1.62	0.00	0.01	0.02	0.01	0.00	0.06	0.02	bdl	bdl	bdl	0.00	0.00	101.78
		B_2.12b	56.62	bdl	1.83	26.39	0.02	0.04	0.05	0.13	0.33	0.55	0.32	0.07	0.00	0.00	0.00	0.00	86.34

469

470 **Table 2 (continue).**

	Sample ID	Grain ID	SiO_2	TiO_2	Al_2O_3	FeO	MnO	MgO	CaO	Na_2O	K_2O	P_2O_5	Cl	F	BaO	ZrO_2	O	H2O	TOTAL
Rursee quartz veins	Rursee 2.1 BNV	B_2.1-03	97.91	0.02	0.04	1.69	0.00	0.01	0.00	0.01	0.00	0.00	0.02	bdl	0.00	bdl	0.00	0.00	99.58
		B_2.1-05a	100.31	bdl	0.32	0.19	0.02	0.02	0.00	0.02	0.01	0.00	bdl	bdl	bdl	bdl	0.00	0.00	100.80
		B_2.1-07a	45.73	bdl	0.36	0.11	29.58	0.22	1.79	0.38	1.25	0.02	0.29	bdl	bdl	bdl	0.00	0.00	77.74
		B_2.1-07b	52.22	0.02	0.24	0.05	24.09	0.21	1.52	0.29	0.89	0.00	0.22	bdl	0.03	bdl	0.00	0.00	78.46
		B_2.1-07c	61.70	0.01	0.23	0.10	21.09	0.20	1.21	0.18	0.72	0.01	0.25	bdl	0.02	bdl	0.00	0.00	84.39
		B_2.1-11a	40.79	0.07	26.15	19.64	0.10	3.03	0.01	0.28	3.65	0.03	0.03	0.05	0.12	0.05	0.00	0.00	94.03
		B_2.1-11b	67.46	0.01	15.25	4.91	0.01	0.84	0.07	0.14	3.41	2.12	0.03	0.13	bdl	bdl	0.00	0.00	94.24
	Rursee 3 BPV	B_3.02a	42.77	0.01	15.84	22.60	0.17	4.89	0.07	0.02	0.67	0.07	0.15	bdl	bdl	bdl	0.00	0.00	87.12
		B_3.02b	66.75	0.02	9.82	13.59	0.08	3.14	bdl	0.05	0.17	0.02	0.03	0.00	0.04	0.02	0.00	0.00	93.70
		B_3.02c	90.77	0.02	3.20	3.97	0.03	1.03	bdl	bdl	0.04	0.01	0.00	0.00	0.00	0.05	0.00	0.00	99.08
		B_3.02d	24.66	0.01	21.55	27.73	0.16	6.22	0.06	0.04	0.79	0.53	0.21	0.07	bdl	0.00	0.00	0.00	81.96
		B_3.05a	30.48	0.03	23.88	25.27	0.16	7.25	0.03	0.03	0.29	0.04	0.06	bdl	bdl	bdl	0.00	0.00	87.44
		B_3.05b	39.46	0.00	30.20	13.10	0.06	2.88	0.05	0.16	2.88	0.18	0.10	0.08	bdl	0.09	0.00	0.00	89.24
		B_3.05c	64.23	0.03	16.31	2.75	0.00	1.11	0.01	0.11	4.01	0.01	0.06	bdl	bdl	bdl	0.00	0.00	88.58
		B_3.08a	56.03	0.26	21.87	6.45	0.01	2.10	0.02	0.15	4.74	0.03	0.00	0.09	0.05	bdl	0.00	0.00	91.79
		B_3.08b	70.37	0.01	10.47	12.40	0.05	2.86	0.03	0.00	0.62	0.01	0.02	0.00	0.03	bdl	0.00	0.00	96.82
		B_3.08c	71.23	bdl	15.55	3.49	0.03	0.74	0.04	7.15	0.08	bdl	0.01	0.01	bdl	bdl	0.00	0.00	98.29
		B_3.08d	32.87	0.73	19.01	25.07	0.13	8.40	0.01	0.07	0.09	0.01	0.01	bdl	bdl	0.01	0.00	0.00	86.40
		B_3.11a	64.26	0.01	1.66	9.68	0.06	0.00	0.23	0.33	0.13	0.17	0.16	0.02	0.03	bdl	0.00	0.00	76.76
		B_3.11b	51.24	bdl	12.87	20.70	0.11	4.48	0.01	bdl	0.01	bdl	0.01	0.02	0.03	0.05	0.00	0.00	89.48
	Rursee 4 BPV	B_4.02a	47.91	0.07	3.98	1.07	0.01	0.22	0.58	2.30	2.47	0.15	0.34	0.10	0.06	bdl	0.00	0.00	59.23
		B_4.03	100.84	0.00	bdl	0.02	0.00	0.00	0.02	0.00	0.02	bdl	0.02	bdl	0.08	bdl	0.00	0.00	100.78
		B_4.04	32.13	0.05	3.95	22.69	0.00	0.15	6.00	0.63	0.64	0.17	0.27	0.13	bdl	0.01	0.00	0.00	66.80
		B_4.05	85.80	0.00	0.03	0.01	0.02	0.02	0.32	0.02	0.03	0.24	0.03	bdl	0.71	bdl	0.00	0.00	87.15
		B_4.08	78.34	0.01	0.73	0.04	10.49	0.22	0.96	0.07	0.09	0.00	0.06	bdl	bdl	bdl	0.00	0.00	90.27
	Rursee 5 BNV	B_5-03	60.18	0.12	1.28	1.08	0.05	1.33	3.01	0.98	0.97	0.11	0.37	0.00	bdl	bdl	0.00	0.00	69.38
		B_5-05	96.03	0.12	0.42	0.22	0.03	0.02	0.08	0.07	0.11	0.04	0.01	bdl	0.00	0.00	0.00	0.00	97.09
		B_5-06a	39.40	0.03	5.43	49.86	0.21	0.23	0.17	0.27	0.51	0.93	0.19	0.00	bdl	0.07	0.00	0.00	97.27
		B_5-06b	48.32	0.09	36.38	0.65	0.00	0.66	0.03	0.45	9.16	0.01	0.01	0.10	0.15	bdl	0.00	0.00	95.97
		B_5-06c	47.07	0.05	34.95	0.69	bdl	0.67	0.06	0.35	9.02	0.00	0.02	0.14	0.06	0.06	0.00	0.00	93.12
		B_5-07	83.67	0.01	8.19	0.07	bdl	0.03	0.13	0.09	2.24	0.07	0.03	bdl	bdl	0.00	0.00	0.00	94.48

471

472 **Table 2 (continue).**

	Sample ID	Grain ID	SiO_2	TiO_2	Al_2O_3	FeO	MnO	MgO	CaO	Na_2O	K_2O	P_2O_5	Cl	F	BaO	ZrO_2	O	H2O	TOTAL
Rursee quartz veins	Rursee 6 BPV	B_6-07b	85.19	0.02	8.13	0.00	bdl	bdl	0.12	1.28	0.71	0.07	0.03	bdl	bdl	0.02	0.00	0.00	95.52
		B_6-07a	79.39	0.00	3.32	0.00	0.01	0.03	0.31	0.06	0.94	0.24	0.09	bdl	bdl	bdl	0.00	0.00	84.32
		B_6-16a	49.44	bdl	37.34	0.06	bdl	0.10	0.08	5.13	1.63	0.01	0.02	0.05	0.04	bdl	0.00	0.00	93.85
		B_6-16b	57.16	0.01	19.71	0.03	bdl	0.06	0.16	2.85	1.57	0.03	0.03	bdl	0.05	bdl	0.00	0.00	81.61
		B_6-17	30.47	0.03	21.91	31.64	0.17	6.42	0.01	0.02	bdl	0.02	0.02	bdl	bdl	bdl	0.00	0.00	90.55
		B_6-19	69.23	0.04	17.80	0.12	bdl	0.04	0.04	0.46	4.81	0.00	0.03	0.00	0.01	bdl	0.00	0.00	92.51
Internal standard of UU	KL2-2		50.09	2.55	13.10	10.78	0.17	6.99	10.80	2.33	0.47	0.25	0.00	0.00	0.01	bdl	0.00	0.00	97.49
			50.37	2.59	13.11	10.79	0.14	6.93	10.94	2.42	0.51	0.25	0.00	bdl	0.04	bdl	0.00	0.00	98.00
			50.27	2.65	13.13	10.83	0.16	6.97	10.93	2.30	0.46	0.27	0.01	bdl	bdl	0.01	0.00	0.00	97.95
Internal standard of UU	ATHO-2		74.10	0.23	12.11	3.37	0.10	0.11	1.63	3.60	2.80	0.03	0.05	0.04	0.04	0.02	0.00	0.00	98.23
			74.00	0.24	12.22	3.38	0.10	0.09	1.59	3.60	2.68	0.03	0.04	0.10	0.06	0.01	0.00	0.00	98.13
			74.39	0.21	12.11	3.41	0.10	0.09	1.63	3.55	2.70	0.06	0.04	0.02	0.08	0.08	0.00	0.00	98.48
Internal standard of UU	KL2-3		51.64	2.60	13.46	10.89	0.19	7.46	10.98	2.33	0.47	0.30	0.00	bdl	0.00	0.02	0.00	0.00	100.29
			50.51	2.62	13.24	10.82	0.13	7.29	10.81	2.28	0.48	0.29	0.00	bdl	bdl	0.04	0.00	0.00	98.43
			50.83	2.61	13.13	10.97	0.15	7.29	11.01	2.30	0.48	0.29	0.01	bdl	bdl	0.02	0.00	0.00	99.00
Internal standard of UU	ATHO-3		76.25	0.24	12.22	3.29	0.10	0.09	1.62	3.65	2.77	0.04	0.05	0.06	0.03	0.11	0.00	0.00	100.53
			75.81	0.24	12.01	3.32	0.10	0.10	1.62	3.55	2.76	0.02	0.03	0.04	0.08	bdl	0.00	0.00	99.63
			75.50	0.26	12.08	3.39	0.10	0.11	1.63	3.69	2.68	0.00	0.03	0.08	0.05	0.07	0.00	0.00	99.67

EPMA analysis of crystal lattice of clean fraction of quartz veins grain of Rursee samples (wt.%).

	Veins generation	Grain ID	SiO_2	TiO_2	Al_2O_3	FeO	MnO	MgO	CaO	Na_2O	K_2O	P_2O_5	Cl	F	BaO	ZrO_2	O	H_2O	TOTAL
Rursee quartz veins	Bedding Normal Veins	AH2.1_04	101.97	bdl	0.03	0.00	bdl	0.00	bdl	0.00	0.00	bdl	0.00	0.01	0.00	bdl	0.00		101.91
		AH2.1_05	101.47	0.00	bdl	bdl	0.00	bdl	0.00	0.01	bdl	0.00	0.00	bdl	0.01	0.02	0.00		101.38
		AH2.1_07	101.68	0.00	0.03	bdl	0.00	0.01	bdl	0.01	0.01	0.00	0.01	bdl	0.02	bdl	0.00		101.68
		AH2.1_09	102.02	bdl	bdl	bdl	0.01	0.01	bdl	bdl	0.01	0.00	bdl	bdl	0.00	bdl	0.00		101.89
	Bedding Parallel Veins	AH2_05	102.67	bdl	0.01	bdl	bdl	0.00	0.01	bdl	0.00	bdl	0.00	bdl	0.01	bdl	0.00		102.61
		AH2_06	102.41	0.02	0.08	bdl	bdl	bdl	0.00	0.02	0.01	0.00	0.00	bdl	0.06	bdl	0.00		102.48
		AH2_07	101.69	bdl	0.05	0.00	bdl	0.01	bdl	bdl	bdl	0.01	0.00	bdl	0.00	0.02	0.00		101.61
		AH2_08	101.42	0.01	0.03	0.01	0.00	bdl	0.00	0.00	bdl	0.01	0.01	bdl	bdl	0.07	0.00		101.47
		AH2_09	102.34	0.01	0.04	bdl	0.00	bdl	bdl	bdl	bdl	bdl	0.00	bdl	0.03	bdl	0.00		102.22

* bdl - below detection limit

5 Conclusions

- The analysis of argon isotope patterns and their interpretations (including K/Cl and inverse isochrons) indicate that the main reservoir $^{39}Ar_K$ for geologically meaningful ages originated from the K-bearing minerals (illite-sericite and some possible chlorite) in quartz vein microcracks and/or inclusions cavities and/or crystal lattice of quartz.
- The determination of a primary crystallization age, i.e. Variscan age, for the quartz veins is not feasible owing to the low amount of K in fluid inclusions and the high amount of excess argon within the FIAs resulting in anomalously old apparent ages in the first ~20th crushing steps.
- The reduced K concentration, due to the loss of primary fluid from inclusions and replacement by a lower salinity, lower K fluid, led to bias in the age determination of fluid inclusions. The obtained ages potentially correspond either to incorporation of a secondary generation of low salinity fluid, or a alternatively to contribution of radiogenic argon reservoirs hosted in solid phases related to intergrowth mineral inclusions during the recrystallisation of quartz veins.
- The maximum apparent ages obtained from the quartz samples span the Jurassic-Cretaceous period. The presence of neo-crystallized quartz sub-grains in the veins is due to the local tectonic activity, indicating that this period is corresponds to tectonic activity of the Rhenish massif.

Data availability

All data is included in the text and/or supplementary files.

Author contributions

The manuscript was primarily authored by Akbar Aydin Oglu Huseynov, the corresponding author. Co-authors Prof. Dr. Klaudia F. Kuiper, Em. Prof. Dr. Jan R. Wijbrans, and Dr. Jeroen van der Lubbe made substantial contributions to data interpretation and refinement of the manuscript, significantly enhancing its clarity and depth.

Competing interest

The authors declare that they have no conflict of interest.

Acknowledgement

This study has been funded by the FluidNET Consortium of EU H2020 Marie Skłodowska-Curie Action (No. 956127). We would like to thank Stefan Groen for his assistance in data management and the $^{40}Ar/^{39}Ar$ analysis laboratory, as well as Roel van Elsas for his help in the Mineral Separation Laboratory at VU Amsterdam. We would like to express our gratitude to

Bouke Lacet for preparing the epoxy grain mounts and thin sections and to Eric Hellebrand and Tilly Bouten for the EPMA analysis. Finally, this study would have been impossible without the support of Prof. Dr. Janos L. Urai, who introduced us to the Rursee outcrops, who unfortunately passed away.

Supplementary file 1 Impact of blank correction on age.

Supplementary file 2 K (and thus $^{40}Ar^{*}$) contribution from chlorite is estimated from 2D electron backscattered images.

Supplementary file 3 Analytical data that have been used for $^{40}Ar/^{39}Ar$ dating.

Supplementary file 4 Grain size distribution analysis of separated fluid-rich quartz fraction after crushing.

Figure A1: Raman spectroscopy of fluid inclusion from Rursee quartz veins. **(a)** Microscopic image of an epoxied and polished fluid-rich quartz fraction. The fluid inclusion that underwent Raman analysis is represented by the red box. **(b)** The Raman plot is presented with the wavelength on the x-axis and intensity on the y-axis. The Raman spectra shows a stretching band in the wavelength range of 3000 to 3700 cm^{-1}, which indicates the presence of an aqueous system.

Figure B1: Normal isochron plots of all quartz veins samples.

Table C1: Rursee quartz veins samples J values and MDF with analytical error.

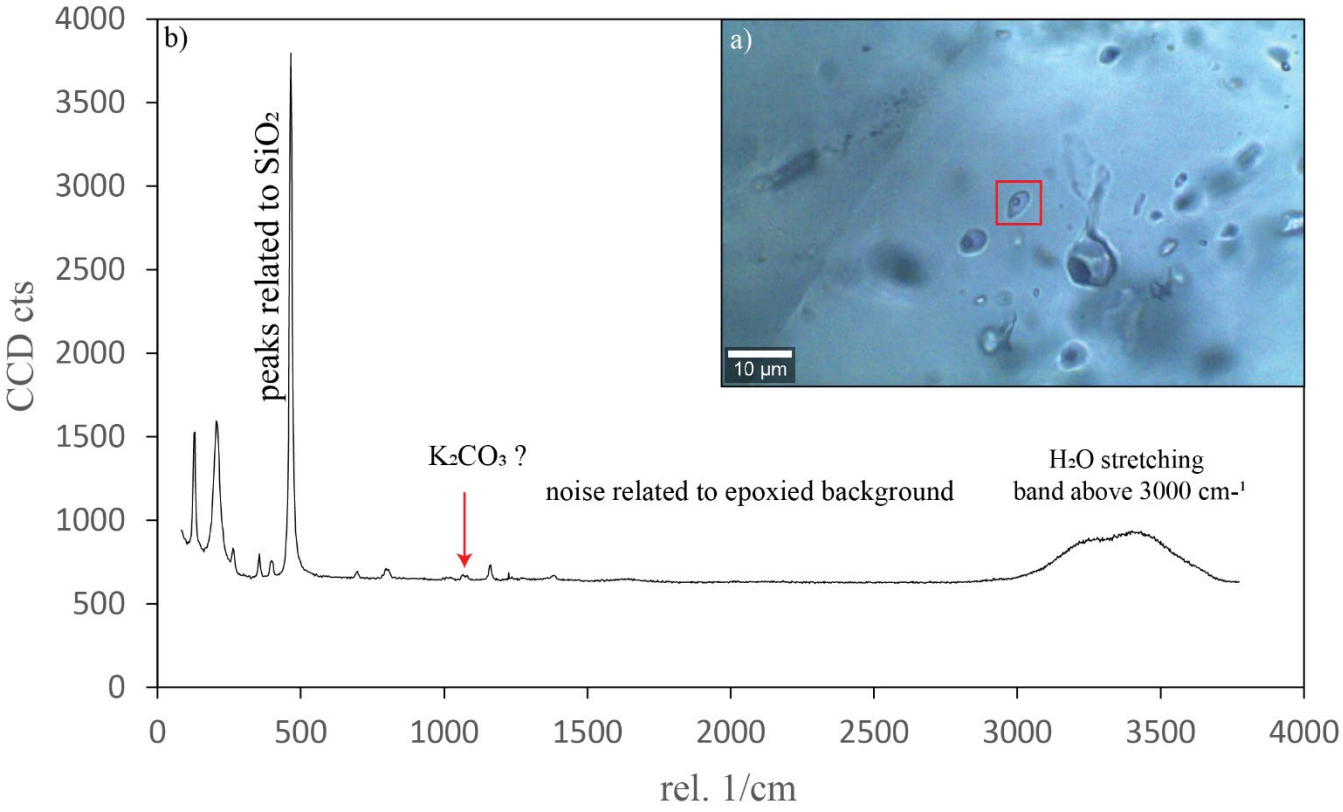

Figure A1: Raman spectroscopy of fluid inclusion from Rursee quartz veins. (a) Microscopic image of an epoxied and polished fluid-rich quartz fraction. The fluid inclusion that underwent Raman analysis is represented by the red box. (b) The Raman plot is presented with the wavelength on the x-axis and intensity on the y-axis. The Raman spectra shows a stretching band in the wavelength range of 3000 to 3700 cm^{-1}, which indicates the presence of an aqueous system.

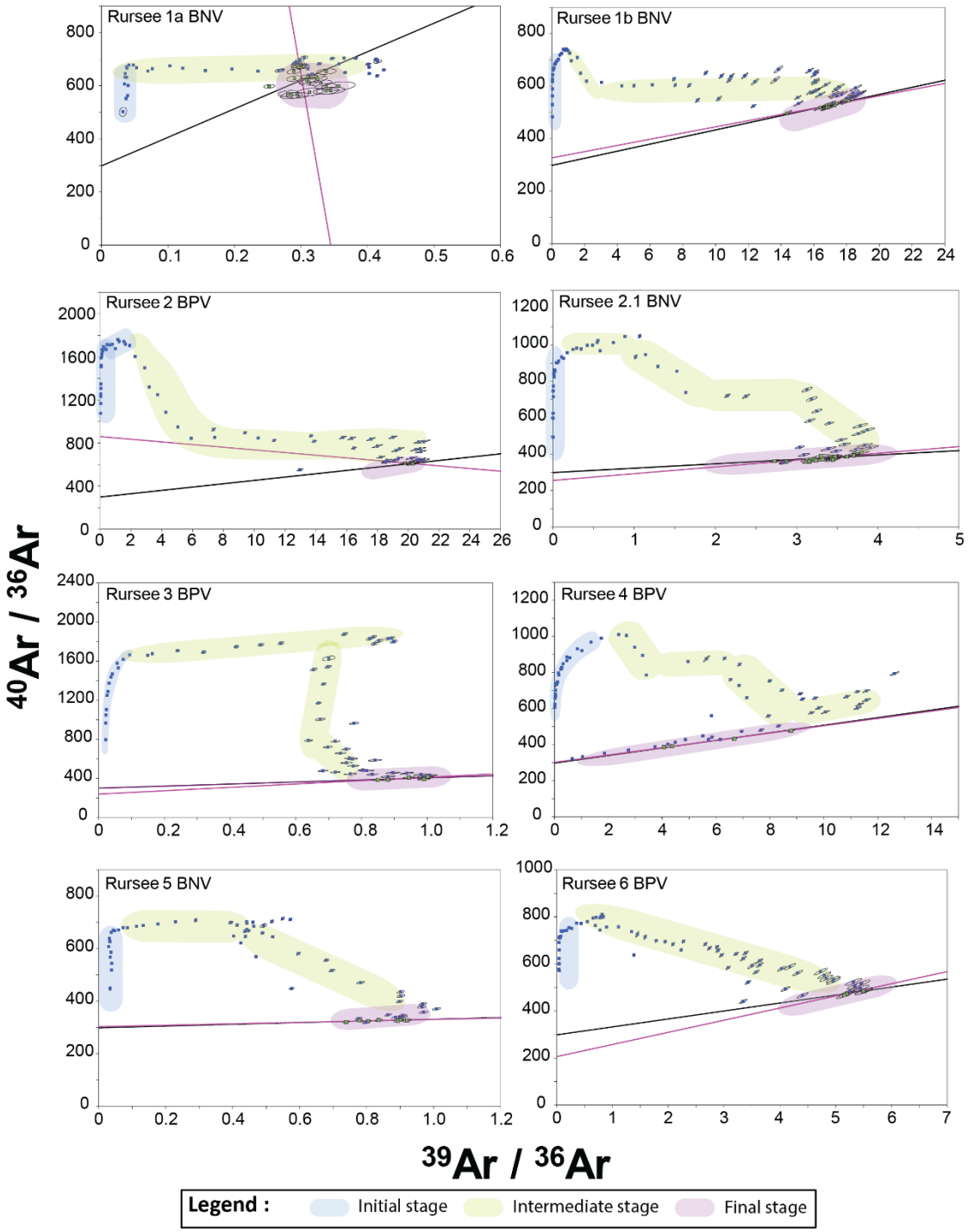

Figure B1: Normal isochron plots of all quartz veins samples.

Table C1: Rursee quartz veins samples J values and MDF with analytical error.

Sample ID	Sample ID Ar	MDF	1σ %	J - value	1σ %
Rursee 1a BNV	R01a	0.99635	± 0.04	0.0034347	± 0.06
Rursee 1b BNV	R01b	0.99519	± 0.04	0.0034737	± 0.06
Rursee 2 BPV	R02	0.99469	± 0.03	0.0035113	± 0.03
Rursee 2.1 BNV	R021	0.99492	± 0.03	0.0034868	± 0.04
Rursee 3 BPV	R03	0.99868	± 0.03	0.0035113	± 0.03
Rursee 4 BPV	R04	0.99749	± 0.03	0.0035113	± 0.03
Rursee 5 BNV	R05	0.99494	± 0.04	0.0034868	± 0.04
Rursee 6 BPV	R06	0.99709	± 0.04	0.0034868	± 0.04

522 **References**

523 Bähr, R. (1987). *Das U Th/He-System in Hämatit als Chronometer für Mineralisationen* (Ph.D. Thesis, University of
524 Heidelberg, Vol. 245, pp. 1–244).

525 Bai, X. J., Wang, M., Jiang, Y. D., & Qiu, H.-N. (2013). Direct dating of tin–tungsten mineralization of the Piaotang tungsten
526 deposit, South China, by $^{40}Ar/^{39}Ar$ progressive crushing. *Geochim. Cosmochim. Acta*, *114*, 1–12.

527 Bai, X. J., Hu, R.-G., Jiang, Y.-D., Liu, X., Tang, B., & Qiu, H.-N. (2019). Refined insight into 40Ar/39Ar progressive crushing
528 technique from K–Cl–Ar correlations in fluid inclusions. *Chemical Geology*, *515*, 37–49.
529 https://doi.org/10.1016/j.chemgeo.2019.03.037

530 Bai X.J., Liu M., Hu R.G., Fang Y., Liu X., Tang B. & Qiu H.N., (2022). Well-Constrained Mineralization Ages by
531 Integrated $^{40}Ar/^{39}Ar$ and U-Pb Dating Techniques for the Xitian W-Sn Polymetallic Deposit, South China:*Economic*
532 *Geology*, 117: 833–852. https://doi.org/10.5382/econgeo.4889.

533 Baksi, A. K. (1994). Geochronological studies on whole-rock basalts, Deccan Traps, India: Evaluation of the timing of
534 volcanism relative to the K-T boundary. *Earth and Planetary Science Letters*, *121*(1), 43–56.
535 https://doi.org/10.1016/0012-821X(94)90030-2

536 Baksi, A. K. (2007). A quantitative tool for detecting alteration in undisturbed rocks and minerals—II: Application to argon
537 ages related to hotspots. In G. R. Foulger & D. M. Jurdy (Eds.), *Plates, Plumes and Planetary Processes* (p. 0).
538 Geological Society of America. https://doi.org/10.1130/2007.2430(16)

539 Ballentine, C. J., Burgess, R., & Marty, B. (2002). Tracing fluid origin, transport and interaction in the crust.
540 https://repository.geologyscience.ru/handle/123456789/29036

541 Bambauer, H. U. (1961). Spurenelementgehalte und g-Farbzentren in Quarzen aus Zerrkluften der Schweizer Alpen.
542 *Schweizerische Mineralogische Und Petrographische Mitteilungen*, *41*, 335–369.

543 Baumgartner, L. P., & Ferry, J. M. (1991). A model for coupled fluid-flow and mixed-volatile mineral reactions with
544 applications to regional metamorphism. *Contributions to Mineralogy and Petrology*, *106*, 273–285.

545 Behr, H.-J., Horn, E. E., Frentzel-Beyme, K., & Reutel, Chr. (1987). Fluid inclusion characteristics of the Variscan and post-
546 Variscan mineralizing fluids in the Federal Republic of Germany. *Chemical Geology*, *61*(1), 273–285.
547 https://doi.org/10.1016/0009-2541(87)90046-5

548 Bonhomme, M. G., Bühmann, D., & Besnus, Y. (1983). Reliability of K-Ar Dating of Clays and Silicifications Associated
549 with vein Mineralizations in Western Europe. *Geologische Rundschau*, *72*(1), 105–117.
550 https://doi.org/10.1007/BF01765902

551 Burnard, P., Graham, D., & Turner, G. (1997). Vesicle-Specific Noble Gas Analyses of 'Popping Rock': Implications for
552 Primordial Noble Gases in Earth. *Science*, *276*(5312), 568–571. https://doi.org/10.1126/science.276.5312.568

Cartwright, I., & Buick, I. S. (2000). Fluid generation, vein formation and the degree of fluid-rock interaction during decompression of high-pressure terranes: The Schistes Lustres, Alpine Corsica, France. *Journal of Metamorphic Geology*, *18*(6), 607–624. Scopus. https://doi.org/10.1046/j.1525-1314.2000.00280.x

Cartwright, J. A., Gilmour, J. D., & Burgess, R. (2013). Martian fluid and Martian weathering signatures identified in Nakhla, NWA 998 and MIL 03346 by halogen and noble gas analysis. *Geochim. Cosmochim. Acta*, *105*(3), 255–293.

Chatziliadou, M., & Kramm, U. (2009). *Rb-Sr Alter und Sr-Pb Isotopencharakteristik von Gangmineralisationen in paläozoischen Gesteinen am Nordrand des linksrheinischen Schiefergebirges (Raum Stolberg-Aachen-Kelmis) und Vergleich mit den rezenten Thermalwässern von Aachen-Burtscheid* (RWTH-CONV-113503, Publikationsserver der RWTH Aachen University). https://publications.rwth-aachen.de/record/51191

Cox, S. F. (2007). Structural and isotopic constraints on fluid flow regimes and fluid pathways during upper crustal deformation: An example from the Taemas area of the Lachlan Orogen, SE Australia. *Journal of Geophysical Research: Solid Earth*, *112*, B08208.

Féraud, G., & Courtillot, V. (1994). Comment on: "Did Deccan volcanism pre-date the Cretaceous-Tertiary transition?" *Earth and Planetary Science Letters*, *122*(1), 259–262. https://doi.org/10.1016/0012-821X(94)90068-X

Fielitz, W. (1995). Epizonal to lower mesozonal diastathermal metamorphism in the Ardennes (Rhenohercynian belt of western central Europe). *Terra Nostra*, *95*(8), 95.

Foland, K. A. (1983). 40Ar/39Ar incremental heating plateaus for biotites with excess argon. *Chemical Geology*, *41*, 3–21. https://doi.org/10.1016/S0009-2541(83)80002-3

Franzke, H. J., & Anderle, H.-J. (1995). Metallogenesis. In R. D. Dallmeyer, W. Franke, & K. Weber (Eds.), *Pre-Permian Geology of Central and Eastern Europe* (pp. 138–150). Springer. https://doi.org/10.1007/978-3-642-77518-5_13

Germann, A., & Friedrich, G. (1999). Strukturkontrollierte, postvariskische Buntmetallmineralisation in paläozoischen und mesozoischen Sedimentgesteinen der nordwestlichen Eifel. *Zeitschrift Der Deutschen Geologischen Gesellschaft*, 513–541.

Glasmacher, U., Zentilli, M., & Grist, A. M. (1998). Apatite Fission Track Thermochronology of Paleozoic Sandstones and the Hill-Intrusion, Northern Linksrheinisches Schiefergebirge, Germany. In P. van den Haute & F. de Corte (Eds.), *Advances in Fission-Track Geochronology: A selection of papers presented at the International Workshop on Fission-Track Dating, Ghent, Belgium, 1996* (pp. 151–172). Springer Netherlands. https://doi.org/10.1007/978-94-015-9133-1_10

Glasmacher, U., Tschernoster, R., Clauer, N., & Spaeth, G. (2001). K–Ar dating of magmatic sericite crystallites for determination of cooling paths of metamorphic overprints. *Chemical Geology*, *175*(3), 673–687. https://doi.org/10.1016/S0009-2541(00)00292-8

Goemaere, E., & Dejonghe, L. (2005). Paleoenvironmental reconstruction of the Mirwart Formation (Pragian) in the Lambert Quarry (Flamierge, Belgium). *Geologica Belgica*, *8*(3), 3–14.

586 Götze, J., Pan, Y., & Müller, A. (2021). Mineralogy and mineral chemistry of quartz: A review. *Mineralogical Magazine*, *85*(5),
587 639–664. https://doi.org/10.1180/mgm.2021.72
588 Heijlen, W., Muchez, P., & Banks, D. A. (2001). Origin and evolution of high-salinity, Zn–Pb mineralising fluids in the
589 Variscides of Belgium. *Mineralium Deposita*, *36*(2), 165–176. https://doi.org/10.1007/s001260050296
590 Hein, U. F., & Behr, H. J. (1994). *Zur Entwicklung von Fluidsystemen im Verlauf der Deformationsgeschichte des*
591 *Rhenoherzynikums*. 191–193.
592 Herbst, F., & Muller, H.-G. (1969). Raum und Bedeutung des Emser Gangzuges. *Gewerkschaft Mercur*.
593 Huseynov, A. A. O., van der Lubbe (Jeroen), H. J. L., Verdegaal-Warmerdam, S. J. A., Postma, O., Schröder, J., & Vonhof, H.
594 (2024). Novel Crushing Technique for Measuring δ18O and δ2H Values of Fluid Inclusions (H2O) in Quartz Mineral
595 Veins Using Cavity Ring-Down Spectroscopy. *Geofluids*, *2024*(1), 5795441. https://doi.org/10.1155/2024/5795441
596 IJlst, L. (1973). A laboratory overflow-centrifuge for heavy liquid mineral separation. *American Mineralogist*, *58*(11–12),
597 1088–1093.
598 Jakobus, R. (1992). Die Erzgänge des östlichen Taunus. *Geol. Jahrb. Hess., 120*, 145–160.
599 Jiang, Y. D., Qiu, H.-N., & Xu, Y. G. (2012). Hydrothermal fluids, argon isotopes and mineralization ages of the Fankou Pb-
600 Zn deposit in south China: Insights from sphalerite 40Ar/39Ar progressive crushing. *Geochim. Cosmochim. Acta*, *84*,
601 369–379.
602 Jourdan, A.-L., Vennemann, T. W., Mullis, J., & Ramseyer, K. (2009). Oxygen isotope sector zoning in natural hydrothermal
603 quartz. *Mineralogical Magazine*, *73*(4), 615–632. https://doi.org/10.1180/minmag.2009.073.4.615
604 Kats, A. (1962). Hydrogen in alpha-quartz. *Philips Res. Rep.*, *17*, 133–195.
605 Kelley, S., Turner, G., Butterfield, A. W., & Shepherd, T. J. (1986). The source and significance of argon isotopes in fluid
606 inclusions from areas of mineralization. *Earth Planet. Sci. Lett.*, *79*(3–4), 303–318.
607 Kendrick, M. A. (2007). Comment on 'Paleozoic ages and excess 40Ar in garnets from the Bixiling eclogite in Dabieshan,
608 China: New insights from 40Ar/39Ar dating by stepwise crushing by Hua-Ning Qiu and J.R. Wijbrans'. *Geochimica*
609 *et Cosmochimica Acta*, *71*, 6040–6045. https://doi.org/10.1016/j.gca.2007.01.029
610 Kendrick, M. A., & Phillips, D. (2009). Discussion of 'the Paleozoic metamorphic history of the Central Orogenic Belt of
611 China from 40Ar/ 39Ar geochronology of eclogite garnet fluid inclusions by Qiu Hua-Ning and Wijbrans J.R.' *Earth*
612 *and Planetary Science Letters - EARTH PLANET SCI LETT*, *279*, 392–394.
613 https://doi.org/10.1016/j.epsl.2008.12.047
614 Kendrick, M. A., Burgess, R., Pattrick, R. A. D., & Turner, P. G. (2001). Halogen and Ar–Ar age determinations of inclusions
615 within quartz veins from porphyry copper deposits using complementary noble gas extraction techniques. *Chem.*
616 *Geol.*, *177*(3–4), 351–370.
617 Kendrick, M. A., Miller, J. M., & Phillips, D. (2006). Part II. Evaluation of 40Ar–39Ar quartz ages: Implications for fluid
618 inclusion retentivity and determination of initial 40Ar/36Ar values in Proterozoic samples. *Geochim. Cosmochim.*
619 *Acta*, *70*(10), 2562–2576.

Kendrick, M. A., Scambelluri, M., Honda, M., & Phillips, D. (2011). High abundances of noble gas and chlorine delivered to the mantle by serpentinite subduction. *Nature Geoscience*, *4*(11), 807–812. https://doi.org/10.1038/ngeo1270

Kirnbauer, T., Wagner, T., Taubald, H., & Bode, M. (2012). Post-Variscan hydrothermal vein mineralization, Taunus, Rhenish Massif (Germany): Constraints from stable and radiogenic isotope data. *Ore Geology Reviews*, *48*, 239–257. https://doi.org/10.1016/j.oregeorev.2012.03.010

Klügel, T. (1997). Geometrie und Kinematik einer variszischen Plattengrenze. Der Südrand des Rhenoherzynikums im Taunus. *Geol. Abh. Hess.*, *101*, 1–215.

Kołtonik, K., Pisarzowska, A., Paszkowski, M., Sláma, J., Becker, R. T., Szczerba, M., Krawczyński, W., Hartenfels, S., & Marynowski, L. (2018). Baltic provenance of top-Famennian siliciclastic material of the northern Rhenish Massif, Rhenohercynian zone of the Variscan orogen. *International Journal of Earth Sciences*, *107*(8), 2645–2669. https://doi.org/10.1007/s00531-018-1628-4

Koppers, A. A. P. (2002). ArArCALC—software for 40Ar/39Ar age calculations. *Computers & Geosciences*, *28*(5), 605–619. https://doi.org/10.1016/S0098-3004(01)00095-4

Korsch, R. J., & Schäfer, A. (1991). Geological interpretation of DEKORP deep seismic reflection profiles 1C and 9N across the variscan Saar-Nahe Basin southwest Germany. *Tectonophysics*, *191*(1), 127–146. https://doi.org/10.1016/0040-1951(91)90236-L

Kučera, J., Muchez, P., Slobodník, M., & Prochaska, W. (2010). Geochemistry of highly saline fluids in siliciclastic sequences: Genetic implications for post-Variscan fluid flow in the Moravosilesian Palaeozoic of the Czech Republic. *International Journal of Earth Sciences*, *99*(2), 269–284. https://doi.org/10.1007/s00531-008-0387-z

Kuiper, K. F., Deino, A., Hilgen, F. J., Krijgsman, W., Renne, P. R., & Wijbrans, J. R. (2008). Synchronizing Rock Clocks of Earth History. *Science*, *320*(5875), 500–504. https://doi.org/10.1126/science.1154339

Lee, J.-Y., Marti, K., Severinghaus, J. P., Kawamura, K., Yoo, H.-S., Lee, J. B., & Kim, J. S. (2006). A redetermination of the isotopic abundances of atmospheric Ar. *Geochimica et Cosmochimica Acta*, *70*(17), 4507–4512. https://doi.org/10.1016/j.gca.2006.06.1563

Li, C., Shen, P., Li, P., Sun, J., Feng, H., & Pan, H. (2022). Changes in the factors controlling the chlorite composition and their influence on hydrothermal deposit studies: A case study from Hongguleleng Manto-type Cu deposit. *Journal of Geochemical Exploration*, *243*, 107096. https://doi.org/10.1016/j.gexplo.2022.107096

Littke, R., Urai, J. L., Uffmann, A. K., & Risvanis, F. (2012). Reflectance of dispersed vitrinite in Palaeozoic rocks with and without cleavage: Implications for burial and thermal history modeling in the Devonian of Rursee area, northern Rhenish Massif, Germany. *International Journal of Coal Geology*, *89*, 41–50. https://doi.org/10.1016/j.coal.2011.07.006

Liu, J., Wu, G., Qiu, H. N., & Li, Y. (2015). 40Ar/39Ar dating, fluid inclusions and S-Pb isotope systematics of the Shabaosi gold deposit, Heilongjiang Province. China. *Geol. J.*, *50*(5), 592–606.

Lo, C.-H., & Onstott, T. C. (1989). 39Ar recoil artifacts in chloritized biotite. *Geochimica et Cosmochimica Acta*, *53*(10), 2697–2711. https://doi.org/10.1016/0016-7037(89)90141-5

Mansy, J. L., Everaerts, M., & De Vos, W. (1999). Structural analysis of the adjacent Acadian and Variscan fold belts in Belgium and northern France from geophysical and geological evidence. *Tectonophysics*, *309*(1), 99–116. https://doi.org/10.1016/S0040-1951(99)00134-1

McKee, E. H., Conrad, J. E., Turrin, B. D., & Theodore, T. G. (1993). 40Ar/39Ar studies of fluid inclusions in vein quartz from Battle Mountain, Nevada. *US Geological Survey Bulletin*, *2039*, 155–165.

Mertz, D. F., Lippolt, H. J., & Müller, G. (1986). Isotopengeochemische (K–Ar, 40Ar/39Ar, Rb–Sr, 87Sr/86Sr) und mineralogische Untersuchungen zur zeitlichen und genetischen Stellung postvariscischer Mineralisationen im Raum Saar-Nahe-Pfalz. *Fortschr. Mineral.*, *64 (Beiheft 1)*, 116.

Min, K., Mundil, R., Renne, P. R., & Ludwig, K. R. (2000). A test for systematic errors in 40Ar/39Ar geochronology through comparison with U/Pb analysis of a 1.1-Ga rhyolite. *Geochimica et Cosmochimica Acta*, *64*(1), 73–98. https://doi.org/10.1016/S0016-7037(99)00204-5

Moe, A. (2000). *Structural development of a volcanic sequence of the Lahn area during the Variscan orogeny in the Rhenohercynian Belt (Germany)* [Dissertation]. https://doi.org/10.11588/heidok.00001095

Mullis, J., Dubessy, J., Poty, B., & O'Neil, J. (1994). Fluid regimes during late stages of a continental collision: Physical, chemical, and stable isotope measurements of fluid inclusions in fissure quartz from a geotraverse through the Central Alps, Switzerland. *Geochimica et Cosmochimica Acta*, *58*(10), 2239–2267. https://doi.org/10.1016/0016-7037(94)90008-6

Oliver, N. H. S., & Bons, P. D. (2001). Mechanisms of fluid flow and fluid–rock interaction in fossil metamorphic hydrothermal systems inferred from vein–wallrock patterns, geometry and microstructure. *Geofluids*, *1*(2), 137–162. https://doi.org/10.1046/j.1468-8123.2001.00013.x

Oncken, O., Von Winterfeld, C., & Dittmar, U. (1999). Accretion of a rifted passive margin: The Late Paleozoic Rhenohercynian fold and thrust belt (Middle European Variscides). *Tectonics*, *18*(1), 75–91.

Onstott, T. C., Miller, M. L., Ewing, R. C., Arnold, G. W., & Walsh, D. S. (1995). Recoil refinements: Implications for the 40Ar/39Ar dating technique. *Geochimica et Cosmochimica Acta*, *59*(9), 1821–1834. https://doi.org/10.1016/0016-7037(95)00085-E

Ozima, M., & Podosek, F. A. (2002). *Noble gas geochemistry*. Cambridge University Press.

Pacey, A., Wilkinson, J. J., & Cooke, D. R. (2020). Chlorite and Epidote Mineral Chemistry in Porphyry Ore Systems: A Case Study of the Northparkes District, New South Wales, Australia. *Economic Geology*, *115*(4), 701–727. https://doi.org/10.5382/econgeo.4700

Perny, B., Eberhardt, P., Ramseyer, K., Mullis, J., & Pankrath, R. (1992). Microdistribution of Al, Li, and Na in α quartz: Possible causes and correlation with short-lived cathodoluminescence. *American Mineralogist*, *77*(5–6), 534–544.

Porat, N. (2006). Use of magnetic separation for purifying quartz for luminescence dating. *Ancient TL*, *24*(2), 33–36.

Potrafke, A., Stalder, R., Schmidt, B. C., & Ludwig, T. (2019). OH defect contents in quartz in a granitic system at 1–5 kbar. *Contributions to Mineralogy and Petrology*, *174*(12), 98. https://doi.org/10.1007/s00410-019-1632-0

Qiu, H.-N. (1996). 40Ar–39Ar dating of the quartz samples from two mineral deposits in western Yunnan (SW China) by crushing in vacuum. *Chem. Geol. (Isot. Geosci Sect.)*, *127*(1–3), 211–222.

Qiu, H.-N., & Dai, T. M. (1989). 40Ar/39Ar techniques for dating the fluid inclusions of quartz from a hydrothermal deposit. *Chin. Sci. Bull.*, *34*(22), 1887–1890.

Qiu, H.-N., & Jiang, Y. D. (2007). Sphalerite 40Ar/39Ar progressive crushing and stepwise heating techniques. *Earth Planet. Sci. Lett.*, *256*(1–2), 224–232.

Qiu, H.-N., & Wijbrans, J. R. (2006). Paleozoic ages and excess 40Ar in garnets from the Bixiling eclogite in Dabieshan, China: New insights from 40Ar/39Ar dating by stepwise crushing. *Geochim. Cosmochim. Acta*, *70*(9), 2354–2370.

Qiu, H.-N., & Wijbrans, J. R. (2008). The Paleozoic metamorphic history of the Central Orogenic Belt of China from 40Ar/39Ar geochronology of eclogite garnet fluid inclusions. *Earth and Planetary Science Letters*, *268*(3), 501–514. https://doi.org/10.1016/j.epsl.2008.01.042

Qiu, H.-N., & Wijbrans, J. R. (2009). Reply to comment by M. A. Kendrick and D. Phillips (2009) on "The Paleozoic metamorphic history of the Central Orogenic Belt of China from 40Ar/39Ar geochronology of eclogite garnet fluid inclusions" by Hua-Ning Qiu and J. R. Wijbrans (2008) [Earth Planet. Sci. Lett. 268 (2008) 501–514]. *Earth and Planetary Science Letters*, *279*(3), 395–397. https://doi.org/10.1016/j.epsl.2009.01.012

Qiu, H.-N., Zhu, B., & Sun, D. (2002). Age significance interpreted from 40Ar–39Ar dating of quartz samples from the Dongchuan copper deposits, Yunnan, SW China, by crushing and heating. *Geochem. J.*, *36*(5), 475–491.

Qiu, H.-N., Wu, H. Y., Yun, J. B., Feng, Z. H., Xu, Y. G., Mei, L. F., & Wijbrans, J. R. (2011). High-precision 40Ar/39Ar age of the gas emplacement into the Songliao Basin. *Geology*, *39*(5), Article 5.

Rama, S. N. I., Hart, S. R., & Roedder, E. (1965). Excess radiogenic argon in fluid inclusions. *J. Geophys. Res.*, *70*(2), 509–511.

Ramsay, J. G. (1986). The techniques of modern structural geology. *The Techniques of Modern Structural Geology, Folds and Fractures*, *2*, 309–700.

Rauchenstein-Martinek, K., Wagner, T., Wälle, M., & Heinrich, C. A. (2014). Gold concentrations in metamorphic fluids: A LA-ICPMS study of fluid inclusions from the Alpine orogenic belt. *Chemical Geology*, *385*, 70–83. https://doi.org/10.1016/j.chemgeo.2014.07.018

Redecke, P. (1992). *Zur Geochemie und Genese variszischer und postvariszischer Buntmetallmineralisation in der Nordeifel und der Niederrheinischen Bucht*. IML.

Schneider, J., & Haack, U. (1997). Rb/Sr dating of silicified wall rocks of a giant hydrothermal quartz vein in the SE Rhenish Massif, Germany. *Proc. 4th Biennial SGA Meeting, Turku*, 971–972.

719 Schneider, J., Haack, U., Hein, U. F., & Germann, A. (1999). Direct Rb–Sr dating of sandstone-hosted sphalerites from
720 stratabound Pb–Zn deposits in the northern Eifel, NW Rhenish Massif, Germany. *Proc. 5th Biennial SGA Meeting*
721 *and 10th Quadrennial IAGOD Symposium, London*, 1287–1290.
722 Schroyen, K., & Muchez, Ph. (2000). Evolution of metamorphic fluids at the Variscan fold-and-thrust belt in eastern Belgium.
723 *Sedimentary Geology*, *131*(3), Article 3. https://doi.org/10.1016/S0037-0738(99)00133-5
724 Schwab, K. (1987). Compression and right-lateral strike-slip movement at the Southern Hunsrück Borderfault (Southwest
725 Germany). *Tectonophysics*, *137*(1), 115–126. https://doi.org/10.1016/0040-1951(87)90318-0
726 Sintubin, M., Kenis, I., Schroyen, K., Muchez, P., & Burke, E. (2000). "Boudinage" in the High-Ardenne slate belt (Belgium),
727 reconsidered from the perspective of the "interboudin" veins. *Journal of Geochemical Exploration*, *69–70*, 511–516.
728 https://doi.org/10.1016/S0375-6742(00)00034-0
729 Stalder, R., Potrafke, A., Billström, K., Skogby, H., Meinhold, G., Gögele, C., & Berberich, T. (2017). OH defects in quartz as
730 monitor for igneous, metamorphic, and sedimentary processes. *American Mineralogist*, *102*(9), 1832–1842.
731 https://doi.org/10.2138/am-2017-6107
732 Sterner, S. M., Hall, D. L., & Bodnar, R. J. (1988). Synthetic fluid inclusions. V. Solubility relations in the system NaCl-KCl-
733 H2O under vapor-saturated conditions. *Geochimica et Cosmochimica Acta*, *52*(5), 989–1005.
734 https://doi.org/10.1016/0016-7037(88)90254-2
735 Sumino, H., Dobrzhinetskaya, L. F., Burgess, R., & Kagi, H. (2011). Deep-mantle-derived noble gases in metamorphic
736 diamonds from the Kokchetav massif. Kazakhstan. *Earth Planet. Sci. Lett.*, *307*(3–4), 439–449.
737 Turner, G., & Bannon, M. P. (1992). Argon isotope geochemistry of inclusion fluids from granite-associated mineral veins in
738 southwest and northeast England. *Geochim. Cosmochim. Acta*, *56*(1), 227–243.
739 Turner, G., & Cadogan, P. H. (1974). Possible effects of 39Ar recoil in 40Ar-39Ar dating. *Proceedings of the Fifth Lunar*
740 *Science Conference, Vol. 2, p. 1601-1615*, *5*, 1601–1615.
741 Turner, G., & Wang, S. S. (1992). Excess argon, crustal fluids and apparent isochrons from crushing K-feldspar. *Earth Planet.*
742 *Sci. Lett.*, *110*(1–4), 193–211.
743 Urai, J. L., Spaeth, G., van der Zee, W., & Hilgers, C. (2001). Evolution of mullion (boudin) structures in the Variscan of the
744 Ardennes and Eifel. *Journal of the Virtual Explorer*, *3*, 1–16.
745 Van Noten, K., Kenis, I., Hilgers, C., Urai, J. L., Muchez, P., & Sintubin, M. (2007). Early vein generations in the High-
746 Ardenne slate belt (Belgium, Germany): The earliest manifestations of the Variscan orogeny? *Géologie de de France*,
747 *2007*(2), 170. https://lirias.kuleuven.be/1929596
748 Van Noten, K., Hilgers, C., L. Urai, J., & Sintubin, M. (2008). Late burial to early tectonic quartz veins in the periphery of the
749 High-Ardenne slate belt (Rursee, north Eifel, Germany). *Geologica Belgica*. https://popups.uliege.be/1374-
750 8505/index.php?id=2485

751 Van Noten, K., Berwouts, I., Muchez, P., & Sintubin, M. (2009). Evidence of pressure fluctuations recorded in crack-seal veins
752 in low-grade metamorphic siliciclastic metasediments, Late Palaeozoic Rhenohercynian fold-and-thrust belt
753 (Germany). *Journal of Geochemical Exploration*, *101*(1), 106. https://doi.org/10.1016/j.gexplo.2008.11.040
754 Van Noten, K., Muchez, P., & Sintubin, M. (2011). Stress-state evolution of the brittle upper crust during compressional
755 tectonic inversion as defined by successive quartz vein types (High-Ardenne slate belt, Germany). *Journal of the*
756 *Geological Society*, *168*(2), Article 2. https://doi.org/10.1144/0016-76492010-112
757 Villa, I. M. (1997). Direct determination of 39Ar recoil distance. *Geochimica et Cosmochimica Acta*, *61*(3), 689–691.
758 https://doi.org/10.1016/S0016-7037(97)00002-1
759 Virgo, S., Abe, S., & Urai, J. L. (2013). Extension fracture propagation in rocks with veins: Insight into the crack-seal process
760 using Discrete Element Method modeling. *J. Geophys. Res. Solid Earth*, *118*, 5236–5251.
761 https://doi.org/10.1002/2013JB010540
762 Watson, E. B., & Cherniak, D. J. (2003). Lattice diffusion of Ar in quartz, with constraints on Ar solubility and evidence of
763 nanopores. *Geochimica et Cosmochimica Acta*, *67*(11), Article 11. https://doi.org/10.1016/S0016-7037(02)01340-6
764 Weil, J. A. (1984). A review of electron spin spectroscopy and its application to the study of paramagnetic defects in crystalline
765 quartz. *Physics and Chemistry of Minerals*, *10*(4), 149–165. https://doi.org/10.1007/BF00311472
766 Wijbrans, J. R., Pringle, M. S., Koppers, A. a. P., & Scheveers, R. (1995). Argon geochronology of small samples using the
767 Vulkaan argon laserprobe. *Proceedings of the Royal Netherlands Academy of Arts and Sciences*, *2*(98), 185–218.
768 Winterfeld, C.-H. von. (1994). Variszische Deckentektonik und devonische Beckengeometrie der Nordeifel–ein quantitatives
769 Modell. *Aachener Geowiss. Beitr*, *2*, 319.
770 Yardley, B. W. D. (1983). Quartz veins and devolatilization during metamorphism. *Journal of the Geological Society*, *140*(4),
771 657–663. Scopus. https://doi.org/10.1144/gsjgs.140.4.0657
772 Yardley, B. W. D., & Bottrell, S. H. (1993). Post-metamorphic gold quartz veins from NW Italy—The composition and origin
773 of the ore fluid. *Mineralogical Magazine*, *57*, 407–422.
774 Ziegler, P. A., & Dèzes, P. (2005). Evolution of the lithosphere in the area of the Rhine Rift System. *International Journal of*
775 *Earth Sciences*, *94*(4), 594–614. https://doi.org/10.1007/s00531-005-0474-3